The Astrophysical Journal, 748:56 (22pp), 2012 March 20 doi:10.1088/0004-637X/748/1/56

WEAK LENSING MEASUREMENT OF GALAXY CLUSTERS IN THE CFHTLS-WIDE SURVEY

HuanYuan Shan[1,2,3], Jean-Paul Kneib[2], Charling Tao[1,3], Zuhui Fan[4], Mathilde Jauzac[2], Marceau Limousin[2,5], Richard Massey[6], Jason Rhodes[7,8], Karun Thanjavur[9,10,11], and Henry J. McCracken[12]

[1] Department of Physics and Tsinghua Center for Astrophysics, Tsinghua University, Beijing, 100084, China; shanhuany@gmail.com
[2] Laboratoire d'Astrophysique de Marseille, CNRS-Université de Provence, 38 rue Frédéric Joliot-Curie, F-13388 Marseille Cedex 13, France
[3] Centre de Physique des Particules de Marseille, CNRS/IN2P3-Luminy and Université de la Méditerranée, Case 907, F-13288 Marseille Cedex 9, France
[4] Department of Astronomy, Peking University, Beijing, 100871, China
[5] Dark Cosmology Centre, Niels Bohr Institute, University of Copenhagen, Juliane Maries Vej 30, DK-2100 Copenhagen, Denmark
[6] Institute for Astronomy, Royal Observatory, Blackford Hill, Edinburgh EH9 3HJ, UK
[7] California Institute of Technology, MC 350-17, 1200 East California Boulevard, Pasadena, CA 91125, USA
[8] Jet Propulsion Laboratory, California Institute of Technology, Pasadena, CA 91109, USA
[9] Canada France Hawaii Telescope, 65-1238 Mamalahoa Hwy, Kamuela, HI 96743, USA
[10] Department of Physics & Astronomy, University of Victoria, Victoria, BC, V8P 1A1, Canada
[11] National Research Council of Canada, Herzberg Institute of Astrophysics, 5071 West Saanich Road, Victoria, BC, V9E 2E7, Canada
[12] Institude d'Astrophysique de Paris, UMR 7095, 98 bis Boulevard Arago, F-75014 Paris, France
Received 2011 August 9; accepted 2012 January 3; published 2012 March 6

ABSTRACT

We present the first weak gravitational lensing analysis of the completed Canada–France–Hawaii Telescope Legacy Survey (CFHTLS). We study the 64 deg^2 W1 field, the largest of the CFHTLS-Wide survey fields, and present the largest contiguous weak lensing convergence "mass map" yet made. 2.66 million galaxy shapes are measured, using the Kaiser Squires and Broadhurst Method (KSB) pipeline verified against high-resolution *Hubble Space Telescope* imaging that covers part of the CFHTLS. Our i'-band measurements are also consistent with an analysis of independent r'-band imaging. The reconstructed lensing convergence map contains 301 peaks with signal-to-noise ratio $\nu > 3.5$, consistent with predictions of a ΛCDM model. Of these peaks, 126 lie within 3.′0 of a brightest central galaxy identified from multicolor optical imaging in an independent, red sequence survey. We also identify seven counterparts for massive clusters previously seen in X-ray emission within 6 deg^2 XMM-LSS survey. With photometric redshift estimates for the source galaxies, we use a tomographic lensing method to fit the redshift and mass of each convergence peak. Matching these to the optical observations, we confirm 85 groups/clusters with $\chi^2_{\rm reduced} < 3.0$, at a mean redshift $\langle z_c \rangle = 0.36$ and velocity dispersion $\langle \sigma_c \rangle = 658.8\,{\rm km\,s^{-1}}$. Future surveys, such as DES, LSST, KDUST, and EUCLID, will be able to apply these techniques to map clusters in much larger volumes and thus tightly constrain cosmological models.

Key words: cosmology: observations – galaxies: clusters: general – gravitational lensing: weak – X-rays: galaxies: clusters

Online-only material: color figures

1. INTRODUCTION

Clusters of galaxies are the largest gravitationally bound structures in the universe. The number and mass of the biggest clusters are highly sensitive to cosmological parameters including the mass density Ω_m, the normalization of the mass power spectrum σ_8 (e.g., Press & Schechter 1974; Frenk et al. 1990; Eke et al. 1996; Sheth & Tormen 1999), and the dynamics of dark energy (e.g., Bartelmann et al. 2006; Francis et al. 2009; Grossi & Springel 2009). Understanding the properties of clusters is vital to test theories of structure formation and to map the distribution of cosmic matter on scales of ∼1–10 Mpc.

Theoretical predictions of structure formation deal directly with the total mass of clusters; measurements are restricted to indirect proxies that can be observed. Contaminating the translation between theory and observation are large uncertainties in the interpretation of galaxy richness, X-ray luminosity/temperature, and the Sunyaev–Zeldovich decrement (e.g., Bode et al. 2007; Leauthaud et al. 2010). Weak gravitational lensing, the coherent distortion of galaxies behind a cluster, can potentially provide direct measurements of the total mass regardless of its baryon content, dynamical state, and star formation history.

By measuring the shear (coherent elongation) of many background galaxies, we can reconstruct the two-dimensional (2D) weak lensing convergence map, which is proportional to density projected along each line of sight. Peaks in the convergence map with high signal-to-noise ratio ν generally correspond to massive clusters (Hamana et al. 2004; Haiman et al. 2004). Since the three-dimensional (3D) shear signal should increase behind those clusters in a predictable way that depends upon only the lens-source geometry, we can also use photometric redshift estimates of the background galaxies (from multi-band imaging) to measure the redshift and mass of each foreground cluster (Wittman et al. 2001, 2003; Hennawi & Spergel 2005; Gavazzi & Soucail 2007).

Systematic weak lensing cluster searches have only recently become practicable. Miyazaki et al. (2002) used Subaru/Suprime-Cam in excellent seeing conditions to find an excess of 4.9 ± 2.3 convergence peaks with $\nu > 5$ in an area of 2.1 deg^2. Dahle et al. (2003) and Schirmer et al. (2003) each identified several shear-selected clusters with redshifts $z \sim 0.5$ determined from two-color photometry. Hetterscheidt et al. (2005) reported the detection of five cluster candidates over a set of 50 disconnected Very Large Telescope/ FORS images covering an effective area of 0.64 deg^2, while Wittman et al. (2006) found eight detections in the first 8.6 deg^2 of the *Blanco* Deep Lens Survey. Gavazzi & Soucail (2007) presented a weak lensing analysis of initial Canada–France–Hawaii Telescope Legacy Survey (CFHTLS) Deep data covering 4 deg^2. They demonstrated that the image quality at CFHT is easily

sufficient for cluster finding. Miyazaki et al. (2007) presented the first large sample of weak-lensing-selected clusters in the Subaru weak lensing survey, with 100 significant convergence peaks in a 16.7 deg^2 effective survey area. Hamana et al. (2009) reported results from a multi-object spectroscopic campaign to target 36 of these cluster candidates, 28 of which were confirmed (and 6 were projections along a line of sight of multiple small groups).

The main astrophysical systematic effect afflicting weak lensing cluster surveys is the projection of large-scale structures along the line of sight. Random noise is also added due to the finite density of resolved source galaxies and the scatter of their intrinsic shapes. Numerical studies (White et al. 2002; Hamana et al. 2004) show that these contaminants significantly reduce the purity of cluster detection. To improve our analysis, we shall combine our weak lensing results with multi-wavelength imaging. Simultaneous detection of a weak lensing signature plus an overdensity of galaxies with a single red sequence provides an unambiguous cluster identification. Furthermore, 3D lensing tomography using photometric redshifts from the multi-wavelength data can remove the other potential hurdles, for example, lensing signal dilution by cluster member galaxies and identifying the redshift of weak lensing peaks when no corresponding galaxy overdensity is apparent.

In this paper we present a weak gravitational lensing analysis of the 64 deg^2 CFHTLS-Wide W1 field, which is sufficiently large to contain several hundred galaxy clusters. Compared to the analysis of the CFHTLS-Deep survey by Gavazzi & Soucail (2007), our shallower CFHTLS-Wide imaging (and lower source galaxy density) will favor the detection of higher mass, nearby clusters. The huge increase in survey area over any previous survey is expected to yield many more systems overall. In this paper, we shall primarily study the properties of the detected clusters, rather than the cosmology in which they are embedded. For this purpose, we adopt a default cosmological model with $\Omega_m = 0.27$, $\Omega_\Lambda = 0.73$, $\sigma_8 = 0.809$, $H_0 = 100\,h\,\mathrm{km\,s^{-1}\,Mpc^{-1}}$, and $h = 0.71$.

This paper is organized is follows. In Section 2, we describe the CFHT and *Hubble Space Telescope* (*HST*) data used. In Section 3, we present the measurement of galaxy shapes in the CFHT imaging, and their calibration against measurements of the same galaxies in the *HST* imaging. In Section 4, we reconstruct the 2D lensing convergence "mass map" signal and extract a catalog of local maxima that represent cluster candidates. In Section 5, we search for optical counterparts of these candidates, dramatically cleaning the catalog. In Section 6, we investigate the full 3D lensing signal around each cluster, further cleaning the catalog when the lensing signal behind spurious peaks does not increase as expected with redshift—but obtaining an independent estimate of the cluster redshift when it does. We finally explore global scaling relations between cluster mass observables, then conclude in Section 7.

2. DATA

2.1. CFHTLS-Wide T0006 Imaging

The CFHT Legacy Survey is a joint Canadian–French program to make efficient use of the CFHT wide field imager MegaPrime, simultaneously addressing several fundamental questions in astronomy. Each MegaPrime/MegaCam image consists of an array of 9 × 4 e2v CCDs with a pixel scale of 0.″187 and a total field of view of ∼1 deg^2. The survey used most of the telescope dark and gray time from 2003 to 2008. We analyze CFHTLS-Wide imaging from the Terapix T0006 processing run, which is the first to include the complete survey and was publicly released on 2010 November 15 (Goranova et al. 2009). These data cover ∼171 deg^2 in four fields (W1, W2, W3, and W4) of which the 72-pointing, ∼64 deg^2 W1 field is the largest, and in five passbands (u', g', r', i', and z') down to $i \sim 24.5$ and $r \sim 25.0$.

Fu et al. (2008) showed that the i'-band exposures, taken in subarcsecond seeing conditions, provide the best image quality and resolve the galaxy population with highest median redshift. Resolving the shapes of more distant galaxies is vital for weak lensing analysis, since the strength of the shear signal is proportional to the ratio of the Lens–Source and Observer–Source distances. We therefore choose to analyze the i'-band images (mean seeing 0.″73) in the contiguous W1 field. We also analyze the independent r'-band imaging to check the calibration of our shear measurements. We also use photometric redshift estimates for source galaxies obtained from the multicolor imaging (Ilbert et al. 2006; Coupon et al. 2009; Arnouts et al. 2010).

Early releases of smaller regions of the CFHTLS have also been used to measure the weak lensing cosmic shear signal (Semboloni et al. 2006; Hoekstra et al. 2006; Fu et al. 2008). As the survey size has increased, the statistical errors have shrunk, and difficulty measuring shapes at a precision better than the statistical error has so far prevented publication of a cosmic shear analysis of the complete survey. However, weak lensing cluster searches are restricted by construction to regions of the survey where the signal is strongest, and the circular symmetry of our analysis removes the negative impact of additive shear measurement errors (cf. Mandelbaum et al. 2005).

2.2. HST COSMOS Imaging

The *HST* COSMOS survey (Scoville et al. 2007) is the largest contiguous optical imaging survey ever conducted from space. High resolution (0.″12) imaging in the I_{F814W} band was obtained during 2003–2005 across an area of 1.64 deg^2 that also corresponds to the CFHTLS D2 deep field. Any galaxies resolved by CFHT are very easily resolved by *HST*, which therefore provides highly accurate shape measurements almost without the need for point-spread function (PSF) correction. We calibrate our CFHTLS shape measurements against those from COSMOS by Leauthaud et al. (2010).

Note that measurements of the shapes of individual galaxies from ground-based and space-based observations need not necessarily match exactly, even without shape measurement errors, because the different noise properties of the data sets may make them most sensitive to different isophotes, which can be twisted relative to each other. The slightly different passbands may also emphasize different regions of a galaxy's morphology. However, across a large population of galaxies, these differences should average out, and a comparison of successful shear measurements between the two data sets should agree.

3. GALAXY SHAPE MEASUREMENT

3.1. Object Detection and Masking

We conduct shape measurement in both CFHTLS i' and r' bands. We detect astronomical sources in the images using SExtractor (Bertin & Arnouts 1996). Our choice of the main SExtractor parameters is listed in Table 1, and the data are filtered prior to detection by a 3 pixel Gaussian kernel.

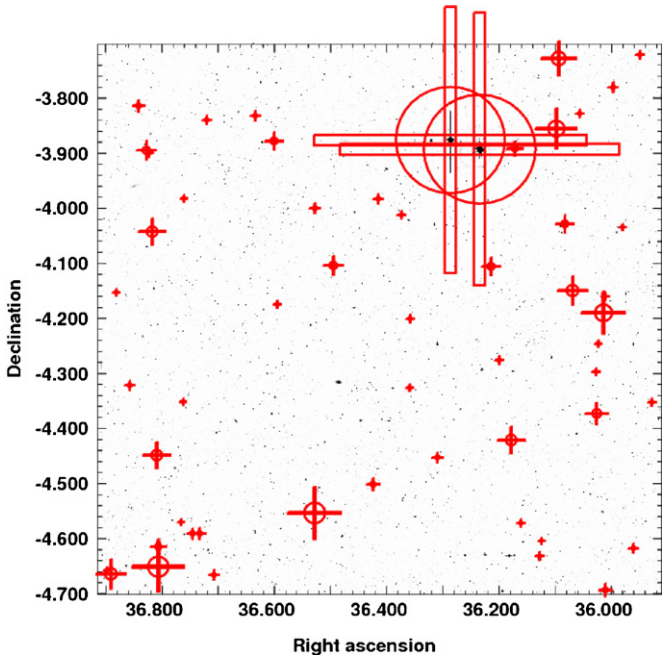

Figure 1. "W1+2+3" pointing from the CFHTLS-Wide W1 field in i' band, showing masked regions. This pointing is representative of those with fairly poor image quality: the seeing of 0.″78 is worse in only 24 of 72 (1 in 3) pointings. In our automated algorithm for masking diffraction spikes around bright stars, the basic shape of the star mask is predefined, and its size is scaled with the observed major axis of each star.

(A color version of this figure is available in the online journal.)

Table 1
SExtractor Configuration Parameters

Parameter	Value
DETECT_MINAREA	3
DETECT_THRESH	1.0
DEBLEND_NTHRESH	32
DEBLEND_MINCONT	0.002
CLEAN_PARAM	1.0
BACK_SIZE	512
BACK_FILTERSIZE	9
BACKPHOTO_TYPE	local
BACKPHOTO_THICK	30

Near saturated stars, many spurious objects are found due to detector effects and optical ghosting. It would also be difficult to measure the shapes of real stars or galaxies in these regions because of the steep background gradients. We have developed an automatic pipeline to define polygonal-shaped masks around saturated stars, and all objects inside the masks are removed from our catalog. The masks in all images are then visually inspected; our automated pipeline fails in a few cases (mainly very saturated stars for which the centroid of the star measured by SExtractor was widely offset from the diffraction spikes) and those stellar masks are corrected by hand. An example of the masks for one CFHT pointing is shown in Figure 1. This pointing has slightly worse than average image quality, so we shall use it throughout this paper as a conservative representation of our analysis. After applying all of our masks across the entire survey, the final effective sky coverage drops from 64 deg^2 to $\sim$51.3 deg^2 and 55.0 deg^2 for i' and r' bands, respectively.

We shall employ the popular KSB method for galaxy shear measurement (Kaiser et al. 1995; Luppino & Kaiser 1997; Hoekstra et al. 1998). In this method, the observed galaxy shape

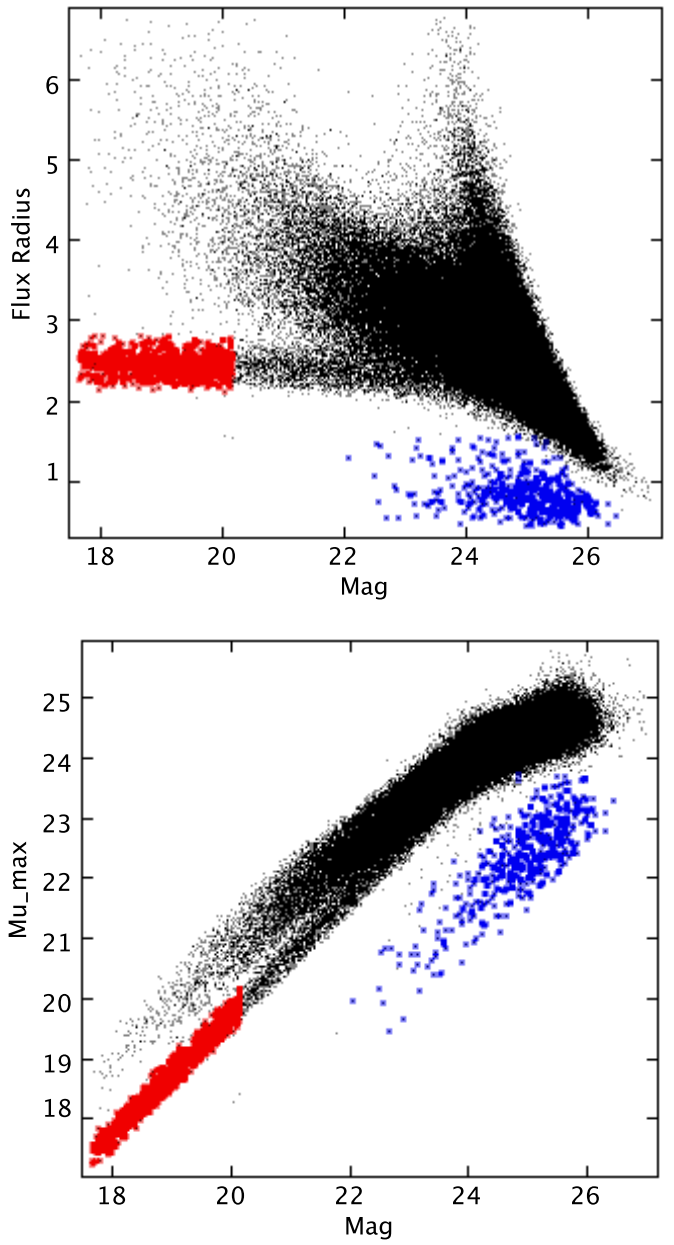

Figure 2. Star selection (red points) in the planes of magnitude vs. flux radius (top) and magnitude vs. peak surface brightness (bottom). We find the latter more robust. The red points denote objects selected as stars for PSF modeling. The blue objects are spurious detection.

(A color version of this figure is available in the online journal.)

is modeled as a convolution of the (sheared) galaxy with the PSF, which is modeled as an isotropic, circular profile convolved with a small anisotropy.

3.2. PSF Modeling

To measure the shapes of galaxies, it is first necessary to correct them for convolution with the PSF imposed by the telescope optics and Earth's atmosphere. The changing size and shape of the PSF across the field of view and between exposures can be traced from stars, which are intrinsically point sources. We identify stars from their constrained locus within the size-magnitude plane (Figure 2(a)). Heymans et al. (2006) suggest using the FWHM. However, we find that the FWHM is not robustly measured by SExtractor, so we

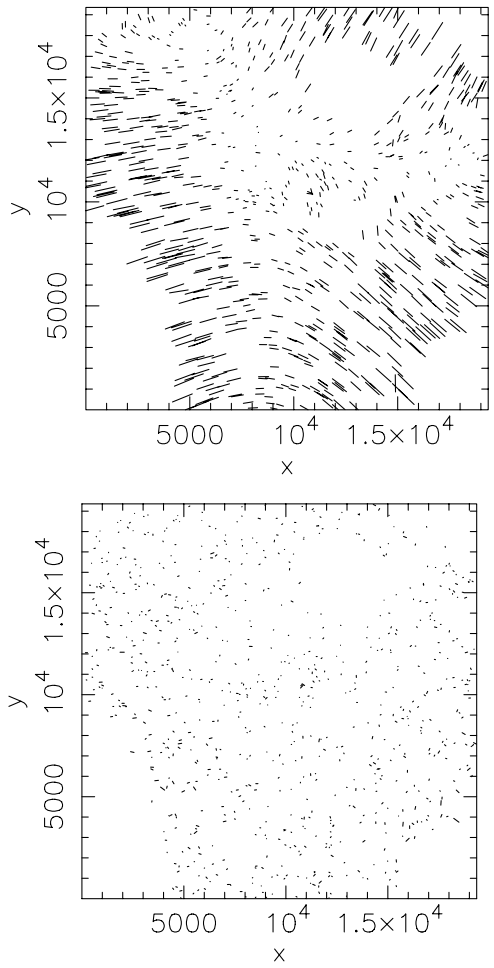

Figure 3. Spatial variation of measured stellar ellipticities in the representative CFHTLS-Wide W1+2+3 field before (top) and after (bottom) PSF anisotropy correction. The longest tick marks represent ellipticities of ∼11%. The mean absolute ellipticity after correction is 0.62%.

instead use the $\mu_{\rm max}$-magnitude plane (Bardeau et al. 2005, 2007; Leauthaud et al. 2007), where $\mu_{\rm max}$ is the peak surface brightness (Figure 2(b)). The red points in Figure 2 indicate the selected stars; our chosen locus reflects a careful balance between obtaining sufficient stars to model the small-scale variations that we observe in the PSF pattern, and introducing spurious noise by including faint stars. The blue points are spurious detections of noise, cosmic rays, etc. (cf. Leauthaud et al. 2007).

We then measure the Gaussian-weighted shape moments of the stars, and construct their ellipticity. In addition to cuts in $\mu_{\rm max}$ and magnitude, we also exclude noisy outliers with signal-to-noise $\nu < 100$ or absolute ellipticity e^* more than 2σ away from the mean local value, and we iteratively remove objects very different from neighboring stars. In 15 pointings with the worst image quality, including W1+2+3, the PSF becomes larger than $r_g \sim 0\farcs5$ in the corners of the field of view, so we finally add these regions to the survey mask (and exclude galaxies in them from our weak lensing analysis).

Having obtained our clean sample of stars, we construct a spatially varying model of the PSF across the field of view. In most pointings, we fit the ∼30 stars in each of the 36 individual CCDs composing the MegaCam focal plane, using a polynomial of second order in x and y. For stacked data with large dithers, we use a higher order polynomial. Figures 3 and 4 show the stellar

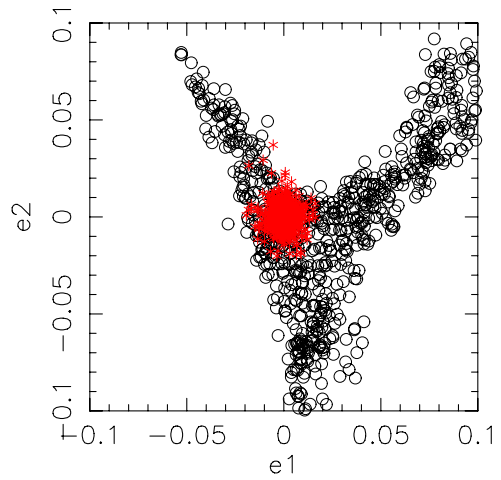

Figure 4. Projection of the stellar ellipticities in the (e_1, e_2) plane before (black) and after (red) PSF anisotropy correction. The post-correction residuals are consistent with featureless white noise.

(A color version of this figure is available in the online journal.)

ellipticity before and after correction for the W1+2+3 pointing, using a weight function of default size r_g to measure the PSF shape moments. The residual stellar ellipticity after correction is a consistent random scatter around zero, of width $\sigma_{e_i} \sim 0.01$.

The ellipticity of the PSF changes from the core to the wings. We measure the PSF shape using differently sized weight functions and, when correcting each galaxy, use the same size weight function to measure both the PSF and galaxy shapes. Figure 5 shows the variation of mean stellar ellipticity as a function of the weight function size r_g, before and after PSF anisotropy correction.

3.3. Galaxy Shape Measurement

Galaxies are selected as those objects with half light radius $1.1r_h^{\rm PSF} < r_h < 4$ pixels, where $r_h^{\rm PSF}$ is the size of the largest star, signal-to-noise $\nu > 10$, magnitude $21.5 < i' < 24.5$, and SExtractor flag FLAGS = 0. To exclude blended or close pairs that could bias ellipticity measurements, we also cut objects with corrected ellipticity $|e_{\rm cor}| > 1$ and pairs of galaxies within $3''$. After survey masking and catalog cuts, the galaxy number density is $n_g \sim 11.5\,{\rm arcmin}^{-2}$ in an area of $A_{i'} \sim 51.3\,{\rm deg}^2$ of i'-band imaging; and $n_g \sim 7.9\,{\rm arcmin}^{-2}$ in $A_{r'} \sim 55.0\,{\rm deg}^2$ of r'-band data. Note that both are lower than the galaxy density $n_g \sim 38\,{\rm arcmin}^{-2}$ obtained in CFHTLS-Deep imaging by Gavazzi & Soucail (2007). This will restrict our detections to generally more massive clusters. Figure 6 shows the magnitude distribution of the galaxies, and the redshift distribution of the 72% (76%) of galaxies selected in the i' (r') bands that also have photometric redshift estimates by Arnouts et al. (2010).

We then measure the shapes of all the selected galaxies. Our implementation of KSB is based on the KSBf90[13] pipeline (Heymans et al. 2006). This has been generically tested on simulated images containing a known shear signal as part of the Shear Testing Programme (STEP; Heymans et al. 2006; Massey et al. 2007) and the Gravitational Lensing Accuracy Testing (GREAT08; Bridle et al. 2010) challenge. In all cases, the method was found to have small and repeatable systematic errors.

If the PSF anisotropy is small, the shear γ can be recovered to first-order from the observed ellipticity $e^{\rm obs}$ of each galaxies

[13] http://www.roe.ac.uk/~heymans/KSBf90/Home.html

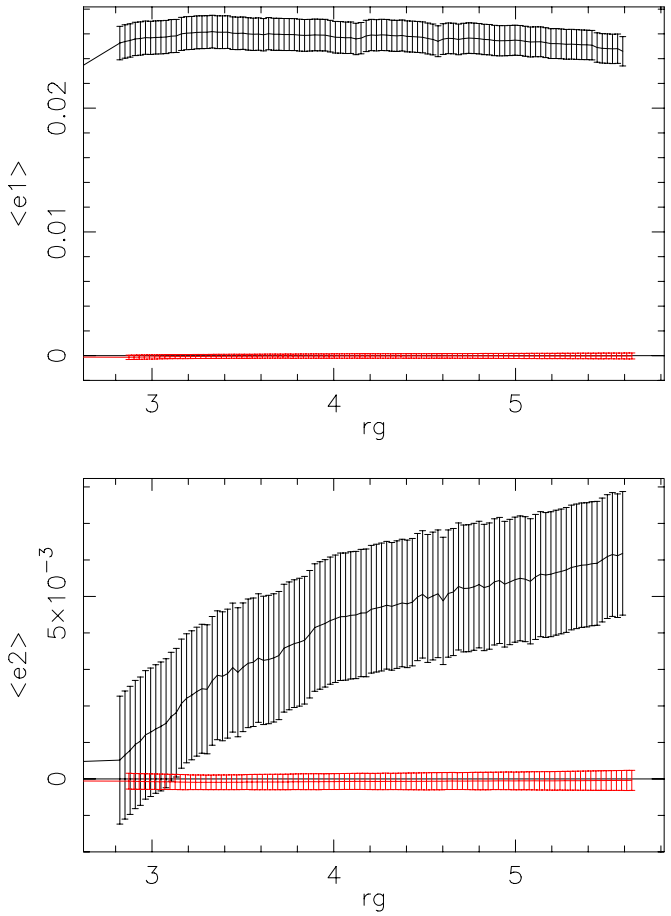

Figure 5. Ellipticity of the PSF changes from the core to the wings. This shows the mean PSF ellipticity in the i'-band of the CFHTLS-Wide W1 pointing W1+2+3 as a function of the size of the Gaussian weight function with which it is measured, before (black) and after (red) PSF anisotropy correction. The error bars show the rms scatter throughout that pointing.

(A color version of this figure is available in the online journal.)

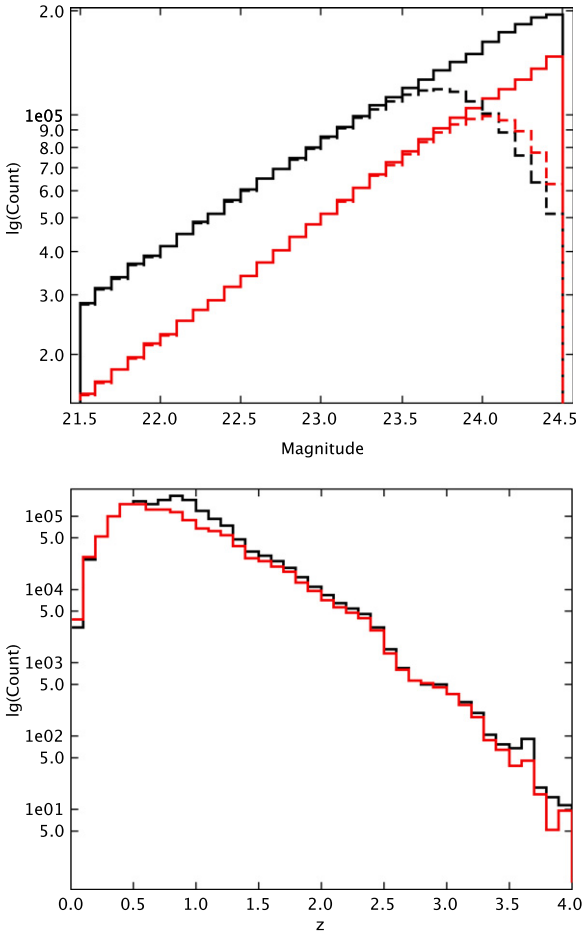

Figure 6. Galaxy magnitude and redshift distributions. Top: number counts of galaxies per magnitude bin immediately after star–galaxy separation (solid histograms) and after all the lensing cuts (dotted histograms) for imaging in i' (black lines) and r' (red lines) bands. Bottom: the redshift distribution of galaxies used from the i' (black lines) and r' (red lines) bands.

(A color version of this figure is available in the online journal.)

via

$$\gamma = P_\gamma^{-1}\left(e^{\rm obs} - \frac{P^{\rm sm}}{P^{\rm sm*}}e^*\right), \quad (1)$$

where asterisks indicate quantities that should be measured from the PSF model interpolated to the position of the galaxy, $P^{\rm sm}$ is the smear polarizability, and P_γ is the correction to the shear polarizability that includes smearing with the isotropic component of the PSF. The ellipticities are constructed from a combination of each object's weighted quadrupole moments, and the other quantities involve higher order shape moments. All definitions are taken from Luppino & Kaiser (1997). Note that we approximate the matrix P_γ by a scalar equal to half its trace. Since measurements of $\mathrm{Tr}\,P_\gamma$ from individual galaxies are noisy, we follow Fu et al. (2008) and fit it as a function of galaxy size and magnitude, which are more robustly observable galaxy properties.

Following Hoekstra et al. (2000), we weight the shear contribution from each galaxy as

$$w = \frac{1}{\sigma_{e,i}^2} = \frac{P_\gamma^2}{\sigma_0^2 P_\gamma + \sigma_{e,i}^2}, \quad (2)$$

where $\sigma_{e,i}$ is the error in an individual ellipticity measurement obtained via the formula in Appendix A of Hoekstra et al. (2000), and $\sigma_0 \sim 0.278$ is the dispersion in galaxies' intrinsic ellipticities.

3.4. Calibration of Multiplicative Shear Measurement Biases

We exploit the opportunity that the CFHTLS-Deep D2 field includes the *HST* COSMOS survey field, and verify the calibration of our shear measurement pipeline for ground-based data against an independent analysis of the much higher resolution space-based data (Leauthaud et al. 2007, 2010). We stack subsets of the CFHTLS-Deep D2 imaging to the same depth as the CFHTLS-Wide survey and analyze it using the same pipeline applied to the CFHTLS-Wide W1 field. Since any galaxy seen by CFHT is very well resolved by *HST*, and imaged to very high signal-to-noise ratio by the COSMOS survey, the space-based shear measurements require only negligible PSF correction and suffer from only negligible shot noise. A consistent shear measurement between ground and space for this subset of galaxies would therefore indicate a robust shear measurement across the CFHTLS.

Multiplicative shear measurement biases m are the most problematic for circularly symmetric cluster measurements. Multiplicative biases cannot be internally diagnosed within a shear catalog, so our comparison against external data is most useful for checking that m is sufficiently small that it

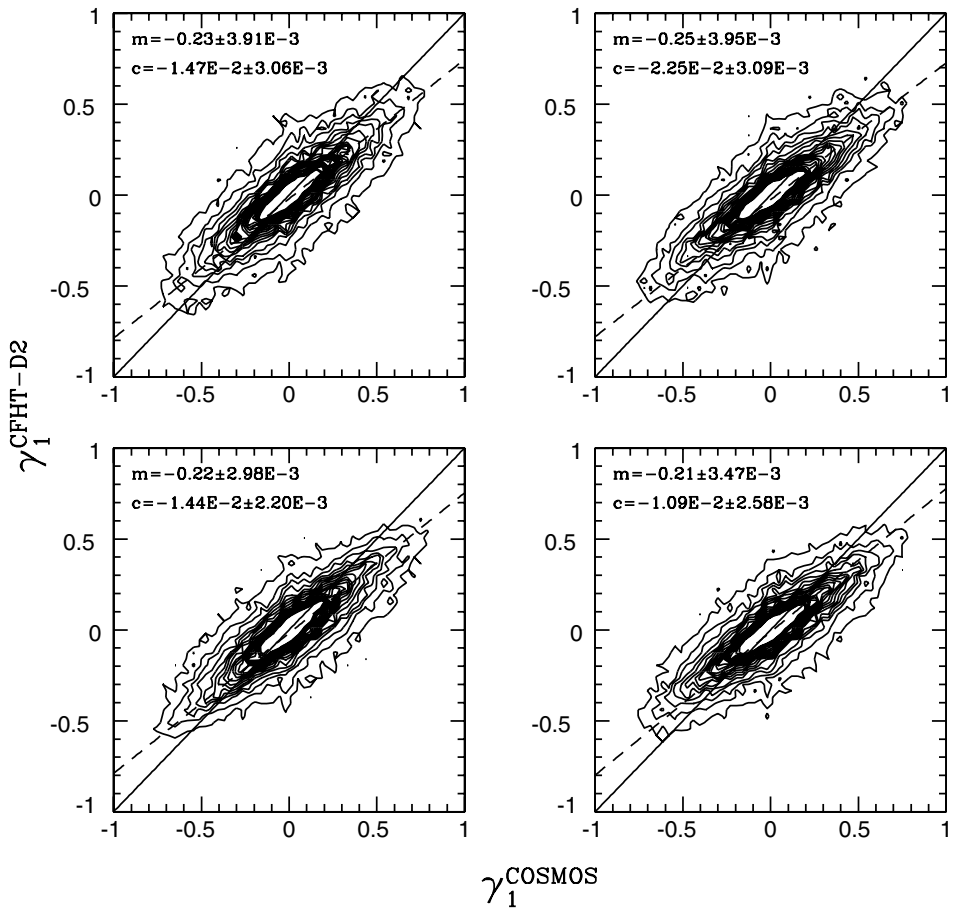

Figure 7. Choices for the way shear polarizability P_γ can be fitted to a galaxy population in the CFHT KSBf90 pipeline to reduce noise and bias in individual measurements. Linearly spaced contours compare our shear measurements of galaxies in a subset of the CFHTLS-Deep imaging, stacked to the depth of the CFHTLS-Wide survey, against measurements from the *Hubble Space Telescope*. Dashed lines show the best-fit relation $\gamma_1^{\rm CFHT} = (m-1)\gamma_1^{HST} + c$. The four panels illustrate various fitting schemes. Top left: raw (noisy) P_γ measurements from each galaxy, without fitting. Top right: fitted as a polynomial in galaxy size $P_\gamma(r_h)$. Bottom-left: fitting function $P_\gamma(r_h, \mathrm{mag})$ from Fu et al. (2008). Bottom-right: best-fit rational function $P_\gamma(r_h, \mathrm{mag})$, as described in the text.

corresponds to a bias smaller than our statistical errors. Within the KSB framework, difficulties in shear calibration mainly rest in measurement of the shear polarizability P_γ, so we first investigate different possibilities for fitting P_γ across a galaxy population. Figure 7 compares shear measurements from a subset of the CFHTLS-Deep imaging with mean seeing 0.″69 (similar to the mean seeing in our survey) stacked to the depth of the CFHTLS-Wide imaging against shear measurements obtained from *HST*. The dashed lines show the best-fit linear relations $\gamma_1^{\rm CFHT} = (1+m)\gamma_1^{HST} + c$, which are obtained using a total least-squares fitting method (e.g., Kasliwal et al. 2008) that accounts for the noise present in both shear catalogs. The top-left panel shows the CFHT shear measurements with P_γ naïvely obtained from each raw, noisy galaxy without any fitting. This results in a large bias on shear measurements and a large amount of extra noise. The top-right panel shows the shear measurements if P_γ is fitted as a function of galaxy size, $P_\gamma(r_h) = a_0 + a_1 r_h + a_2 r_h^2$. The bottom-left panel shows shears if $P_\gamma(r_h, \mathrm{mag}) = a_0 + a_1 r_h + a_2 r_h^2 + a_3 m_v$ (Fu et al. 2008). The bottom-right panel shows the matched shear with $P_\gamma(r_h, \mathrm{mag})$ the best-fit rational function

$$P_\gamma = \frac{a_0 + a_1 m_v + a_2 m_v^2 + a_3 r_h}{1 + a_4 m_v + a_5 m_v^2 + a_6 r_h + a_7 r_h^2}. \quad (3)$$

In this example, the coefficients are $a_0 = 25.07$, $a_1 = -2.19$, $a_2 = 0.045$, $a_3 = 0.53$, $a_4 = 0.58$, $a_5 = -0.022$, $a_6 = -0.85$, and $a_7 = 0.14$. The more sophisticated fits produce a shear catalog that is a marginally better match to the reliable *HST* measurements, and this is even more true if we redo the analysis using the full CFHTLS-Deep depth, in which galaxies are fainter and smaller. We henceforth choose to adopt the rational function fit to P_γ for all subsequent analyses, obtaining new best-fit coefficients for each pointing.

To quantify the performance of our shear measurement pipeline as a function of image quality, we stack subsets of the CFHTLS-Deep D2 imaging with low, medium, and high seeing to the same depth as the CFHTLS-Wide survey and analyze each separately (Figure 8). We find that our CFHTLS pipeline consistently underestimates shear, but that the calibration is remarkably robust to seeing conditions. We can therefore simply recalibrate our pipeline for all images by multiplying all measured shears by 1/(1–0.21).

3.5. Assessment of Residual Additive Shear Systematics

Additive shear measurement systematics c generally cancel out in circularly symmetric cluster measurements (Mandelbaum et al. 2006). However, to double-check for significant additive systematics, we first measure the mean shears $\langle\gamma\rangle$ across all 72 pointings of the CFHTLS-Wide W1 field. Figure 9 demonstrates

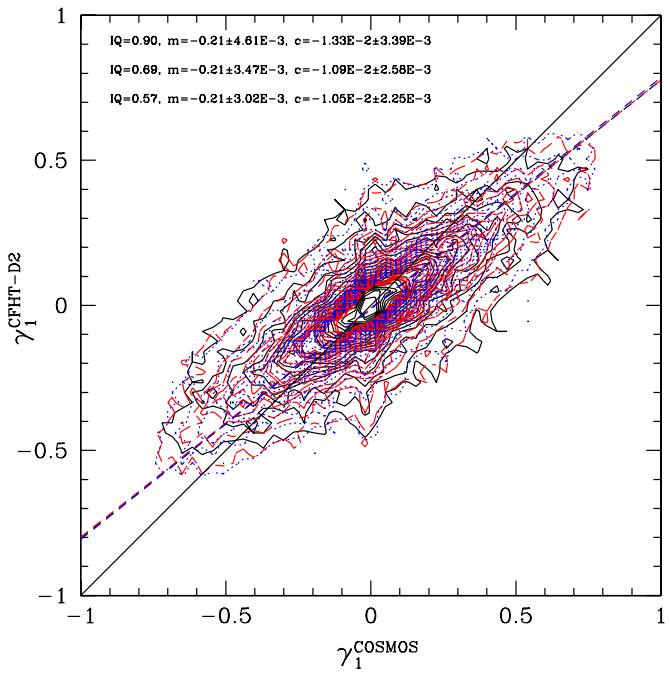

Figure 8. Robustness of the calibration of our shear measurement as a function of image quality. Linearly spaced contours compare our shear measurements of galaxies in subsets of CFHTLS-Deep imaging with varying mean seeing (black solid: 0.″90, red dashed: 0.″69, blue dotted: 0.″57) to measurements from the *Hubble Space Telescope*. Shears are consistently underestimated by our pipeline, but the calibration is remarkably robust.

(A color version of this figure is available in the online journal.)

that the mean shear is consistent with zero as expected for galaxies of all sizes, magnitudes, and signal-to-noise ratios.

We also look for residual systematics left in the weak lensing cosmic shear signal due to imperfect PSF correction. Figure 10 shows the correlation $\xi_{\rm sys}$ between the corrected shapes of galaxies and the uncorrected shapes of stars. Following Bacon et al. (2003) and Massey et al. (2005), we normalize the star–galaxy ellipticity correlation by the uncorrected star–star ellipticity correlation to assess its impact on shear measurements

$$\xi_{\rm sys}(\theta) = \frac{\langle e^*(\mathbf{x})\,\gamma(\mathbf{x}+\theta)\rangle^2}{\langle e^*(\mathbf{x})\,e^*(\mathbf{x}+\theta)\rangle}, \tag{4}$$

where e^* is the ellipticity of the stars before PSF correction and γ is the shear estimate from galaxies. We find that our PSF correction is well within requirements for our analysis because on cluster scales 1–5 arcmin, the amplitude of $\xi_{\rm sys}$ is at least one order of magnitude smaller than the cosmic shear signal

$$\xi_\pm = \xi_{\rm tt}(\theta) \pm \xi_{\rm xx}(\theta) = \frac{1}{2\pi}\int_0^\infty \ell\, P_\kappa(\ell)\, {\rm J}_{0,4}(\ell\theta)\, d\ell, \tag{5}$$

where $\xi_{\rm tt}(\theta)$ ($\xi_{\rm xx}(\theta)$) are the correlation functions between components of shear rotated tangentially (at 45°) to the line between pairs of galaxies separated by an angle θ and $\rm J_0$, $\rm J_4$ are Bessel functions of the first kind.

Because gravitational lensing is achromatic while systematics are typically not, we can also assess the robustness of our measurements by comparing shears measured from independent imaging acquired in multiple bands. The first attempt at comparing multicolor shear measurements was made by Kaiser et al. (2000) using the CFHT12K camera. The *I* and *V* bands showed significantly different signals that were inconsistent with the change in redshift distribution between the two filters. After a great deal of algorithmic progress, Semboloni et al. (2006) obtained consistent shear measurements from i'-band and r'-band CFHTLS-Deep data. Gavazzi & Soucail (2007) extracted consistent shear from the g', r', z' and i' bands of CFHTLS-Deep. Gavazzi et al. (2009) also measured consistent values of the PSF-corrected ellipticities of central Coma cluster galaxies in MegaCam-u^* and CFH12k-*I* bands. Our analysis pipeline measures shears in the independent CFHTLS r'-band and i'-band imaging that are consistent within the ∼0.1 rms noise (Figure 11). To maximize the total number of galaxies in our shear catalog, we therefore combine r'-band and i'-band measurements. Only the unique r'-band galaxies are added to the i'-band catalog. The combined catalog includes ∼2.66 million galaxies, with $n_g \sim 14.5\,{\rm arcmin}^{-2}$ for lensing measurements.

We shall continue testing for systematics at each stage of our analysis by checking that the shear signal behaves as expected and is consistent with external data sets. An important example of this is the (nonphysical) *B*-mode signal, which we shall compute wherever we reconstruct the (physical) *E*-mode. Pure gravitational fields produce zero *B*-mode for isolated clusters and only tiny *B*-modes through coupling between multiple systems along adjacent lines of sight (Schneider et al. 2002). The *B*-mode signal corresponds to the imaginary component of $P_\kappa(\ell)$; it can be conveniently measured by rotating all galaxy shears by 45° then remeasuring the *E*-mode signal (Crittenden et al. 2002).

4. MASS RECONSTRUCTIONS

4.1. Kaiser–Squires Inversion and Masking

The shear field $\gamma_i(\theta)$ is sparsely and noisily sampled by measurements of the shapes of galaxies at positions θ. The smooth, underlying shear field $\gamma_i(\theta)$ can be written in terms of the lensing potential $\phi(\theta)$ as

$$\gamma_1 = \frac{1}{2}\left(\partial_1^2 - \partial_2^2\right)\phi, \tag{6}$$

$$\gamma_2 = \partial_1\partial_2\phi, \tag{7}$$

where the partial derivatives ∂_i are with respect to θ_i. The convergence field $\kappa(\theta)$, which is proportional to the mass projected along a line of sight, can also be expressed in terms of the lensing potential as

$$\kappa = \frac{1}{2}\left(\partial_1^2 + \partial_2^2\right)\phi. \tag{8}$$

We shall reconstruct the convergence field from our shear measurements via the Kaiser & Squires (1993; KS93) method. This is obtained by inverting Equations (6) and (7) in Fourier space:

$$\hat\gamma_i = \hat P_i \hat\kappa \tag{9}$$

for $i = 1, 2$, where the hat symbol denotes Fourier transforms, we define $k^2 = k_1^2 + k_2^2$ and

$$\hat P_1(k) = \frac{k_1^2 - k_2^2}{k^2}, \tag{10}$$

$$\hat P_2(k) = \frac{2k_1k_2}{k^2}. \tag{11}$$

This inversion is non-local, so we deal with masked regions of the shear field by masking out the same area in the convergence

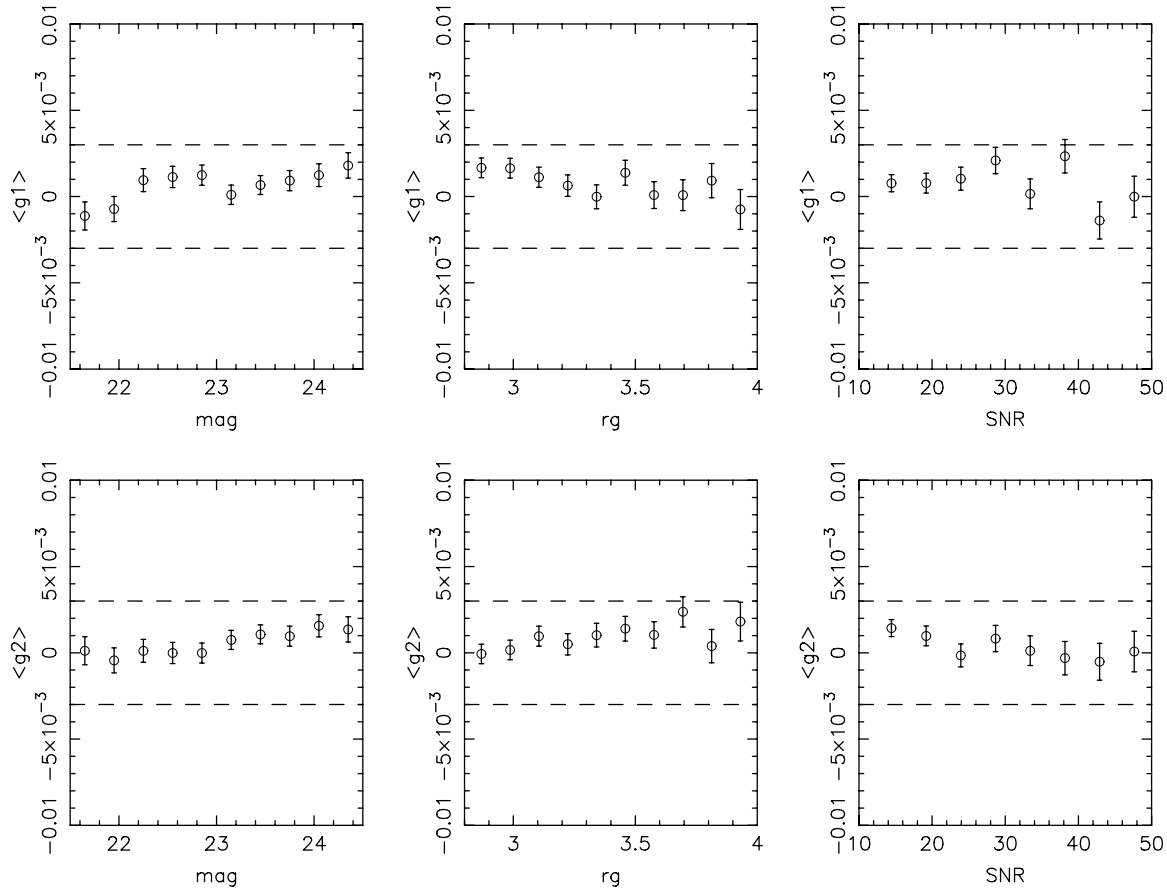

Figure 9. Mean shear measurements from galaxies in i'-band observations of the entire CFHTLS-Wide W1 field. In the absence of additive systematics, these should be consistent with zero. In practice, they always remain within the dashed lines that indicate an order of magnitude lower than the 1%–10% shear signal around clusters. Upper and lower panels show components γ_1 and γ_2, respectively. Left, middle, and right panels show trends as a function of galaxy magnitude, size, and detection signal-to-noise.

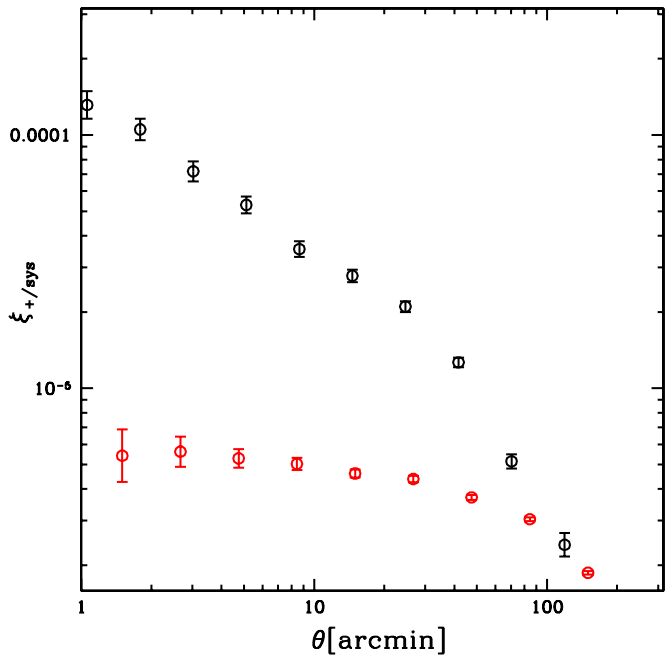

Figure 10. The cross-correlation between shear measurements and stellar ellipticities as a function of the separation between galaxies and stars averaged throughout the CFHTLS-Wide W1 field. If all residual influence of the observational PSF has been successfully removed from the galaxy shape measurements, the red (lower) points should be consistent with zero.

(A color version of this figure is available in the online journal.)

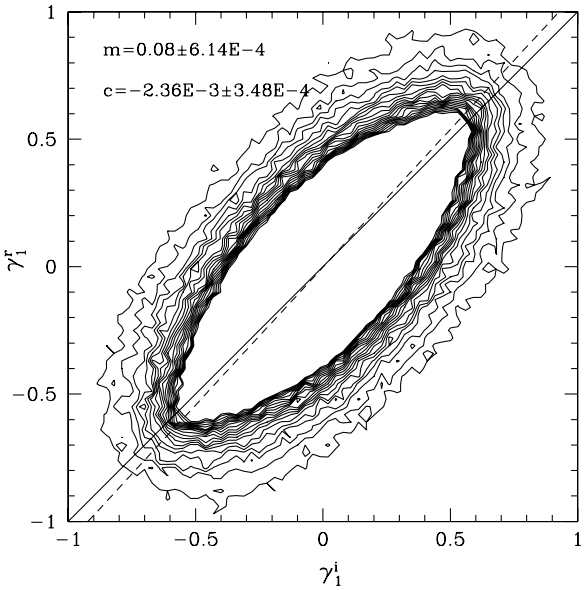

Figure 11. Gravitational lensing is achromatic, so measurements of galaxy shapes from imaging in different colors should on average be consistent. This shows a comparison of shear measurements obtained from CFHTLS-Wide r'-band and i'-band imaging of the whole W1 field. The dashed line shows the best-fit linear relation $\gamma_1^i = (m-1)\gamma_1^r + c$.

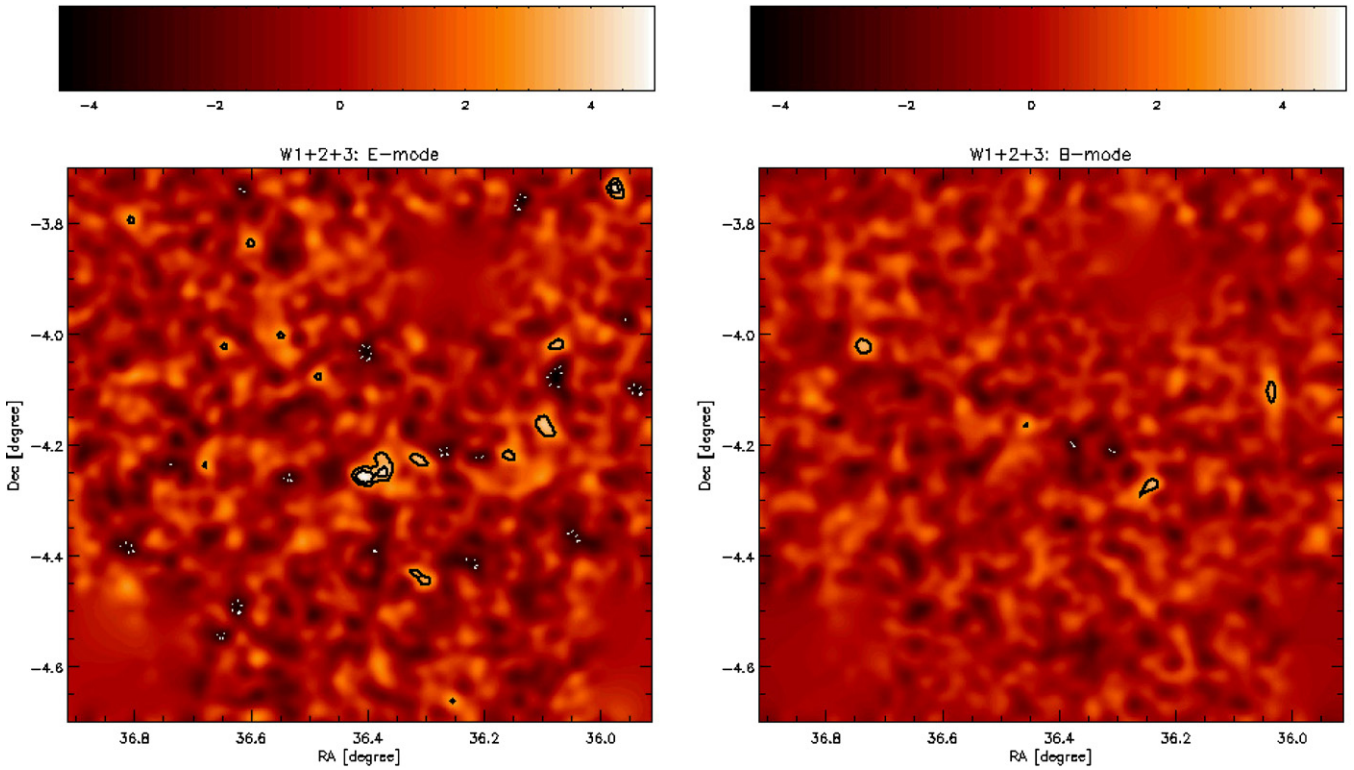

Figure 12. Distribution of foreground mass in the W1+2+3 pointing, reconstructed from shear measurements via the KS93 method. Left: the physical E-mode convergence signal. Right: the B-mode systematics signal, created by rotating the shears by 45° then remaking the map. Contours are drawn at detection significances of 3σ, 4σ, and 5σ, with dashed lines for negative values.

(A color version of this figure is available in the online journal.)

field, plus a 1.′5 border. We shall ignore any signal within these regions and set the convergence to zero in relevant figures.

For the finite density of source galaxies resolved by CFHT, the scatter of their intrinsic ellipticities means that a raw, unsmoothed convergence map $\kappa(\theta)$ will be very noisy. Following Miyazaki et al. (2002), we smooth the convergence map by convolving it (while still in Fourier space) with a Gaussian window function,

$$W_G(\theta) = \frac{1}{\pi\theta_G^2}\exp\left(-\frac{\theta^2}{\theta_G^2}\right). \quad (12)$$

As shown by van Waerbeke (2000), if different galaxies' intrinsic ellipticities are uncorrelated, the statistical properties of the resulting noise field can be described by Gaussian random field theory (Bardeen et al. 1986; Bond & Efstathiou 1987) on scales where the discreteness effect of source galaxies can be ignored. The Gaussian field is uniquely specified by the variance of the noise, which is in turn controlled by the number of galaxies within a smoothing aperture (Kaiser & Squires 1993; Van Waerbeke 2000)

$$\sigma^2_{\rm noise} = \frac{\sigma_e^2}{2}\frac{1}{2\pi\theta_G^2 n_g}, \quad (13)$$

where σ_e is the rms amplitude of the intrinsic ellipticity distribution and n_g is the density of source galaxies. We define the signal-to-noise ratio for weak lensing detections by

$$\nu \equiv \frac{\kappa}{\sigma_{\rm noise}}. \quad (14)$$

To define the noise level in theoretical calculations of ν, we adopt a constant effective density of galaxies equal to the mean within our survey. For observational calculations of ν, we use the mean galaxy density in each pointing—but do not consider the non-uniformity of the density within each field due to masks or galaxy clustering.

A simple Gaussian filter of width $\theta_G \approx 1'$ is close to the optimal linear filter for cluster detection, and this choice has been extensively studied in simulations (White et al. 2002; Hamana et al. 2004; Tang & Fan 2005). Because of our relatively low source galaxy density, the galaxies' random intrinsic shapes will produce spurious noise peaks, degrading the completeness and purity of our cluster detection. To reduce contamination, we repeat our mass reconstruction using two smoothing scales $\theta_G = 1'$ and $\theta_G = 2'$. The map with greater smoothing will be less noisy; to help remove spurious peaks from the higher resolution map, we consider only those peaks detected above a signal-to-noise threshold in both maps.

Figure 12 shows the reconstructed convergence field corresponding to foreground mass in the W1+2+3 pointing. The left panel shows the E-mode reconstruction with KS93 method after smoothing by a 1 arcmin Gaussian kernel. This contains several high signal-to-noise peaks, while the associated B-mode systematics measurement in the right panel is statistically consistent with zero, with fewer peaks. As weak lensing produces only curl-free or E-mode distortions, a detection (significant above statistical noise) of curl or B-mode signal would have indicated contamination from residual systematics, e.g., imperfect PSF correction.

4.2. Large-scale Lensing Mass Map

A reconstructed "dark matter mass" convergence map for the entire 64 deg^2 CFHTLS-Wide W1 field is presented in Figure 13.

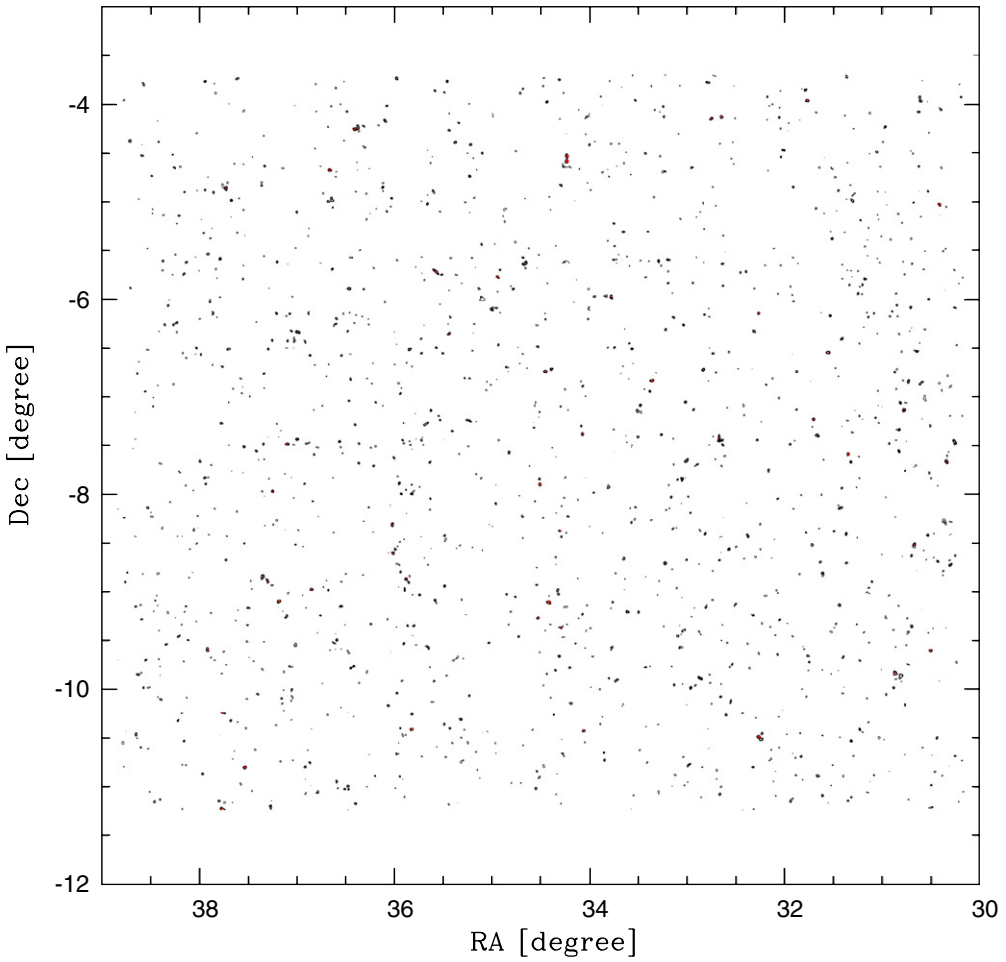

Figure 13. Reconstructed "dark matter mass" convergence map for the entire 64 deg^2 CFHTLS-Wide W1 field. This has been smoothed by a Gaussian filter of width $\theta_G = 1'$. Black contours are drawn at detection signal-to-noise ratios $\nu = 3.0$, 3.5, and 4.0, and red contours continue this sequence from $\nu \geqslant 4.5$.
(A color version of this figure is available in the online journal.)

We detect 301 peaks with $\nu > 3.5$ in maps with both smoothing scales $\theta_G = 1'$ and $\theta_G = 2'$. The same information is reproduced in Figure 14, with $\theta_G = 6'$ and after multi-scale entropy restoration filtering (MRLens; Starck et al. 2006), to better display large-scale features. The MRLens filtering effectively suppresses noise peaks, but results in non-Gaussian noise that complicates the peak selection (Jiao et al. 2011), so we shall not use it further.

To assess the reliability of this map, we shall first investigate the statistical properties of local maxima and minima. Figure 15 shows the distribution of peak heights, as a function of detection signal-to-noise. The bimodal distribution in both the *B*-mode and *E*-mode signals is dominated by positive and negative noise fluctuations, but an asymmetric excess in the *E*-mode signal is apparent at both $\nu > 3.5$ and, at lower significance, $\nu < -3.5$. The amplitude, slope, and non-Gaussianity of this excess are all powerful discriminators between values of parameters in cosmological models (Pires et al. 2009). Positive peaks correspond mainly to dark matter halos around galaxy clusters. Local minima could correspond to voids (Jain & van Waerbeke 2000; Miyazaki et al. 2002), but the large size of voids is ill-matched to our $\theta_G = 1'$ filter width, and their density contrast can never be greater than unity, so this aspect of our data is likely just noise.

Figure 16 recasts the peak distribution into a cumulative density of positive maxima or negative minima. As expected, we find a non-Gaussian mass distribution with more highly significant positive maxima (corresponding to mass overdensities) than highly significant negative minima (see Table 2). Analytic predictions of peak counts are also overlaid. Following van Waerbeke (2000), dot-dashed lines show the expected density of pure noise peaks, and dotted lines show the expected number of true dark matter halos. Predictions from Fan et al. (2010), which also take into account the effect of noise on the heights of true peaks and the clustering of noise peaks near dark matter halos, are shown as circles with error bars. In these theoretical calculations, we model the population of background galaxies as having an intrinsic ellipticity dispersion $\sigma_e = 0.278$, density $n_g = 14.5$ arcmin^{-2}, and the redshift distribution from Fu et al. (2008) in a ΛCDM universe. At $\nu > 4.5$, it appears that theory may begin to predict more peaks than are observed. However, these are very small number statistics, and our observations are

Table 2
The Number of Local Maxima and Minima in the Convergence Map of the CFHTLS-Wide W1 Field as a Function of Smoothing Scale

Smoothing Scale θ_G	*E*-mode $\nu > 3.5$	*E*-mode $\nu < -3.5$	*B*-mode $\nu > 3.5$	*B*-mode $\nu < -3.5$
0.′5	1512	1270	1244	1033
1.′0	543	445	361	282
2.′0	281	233	148	126

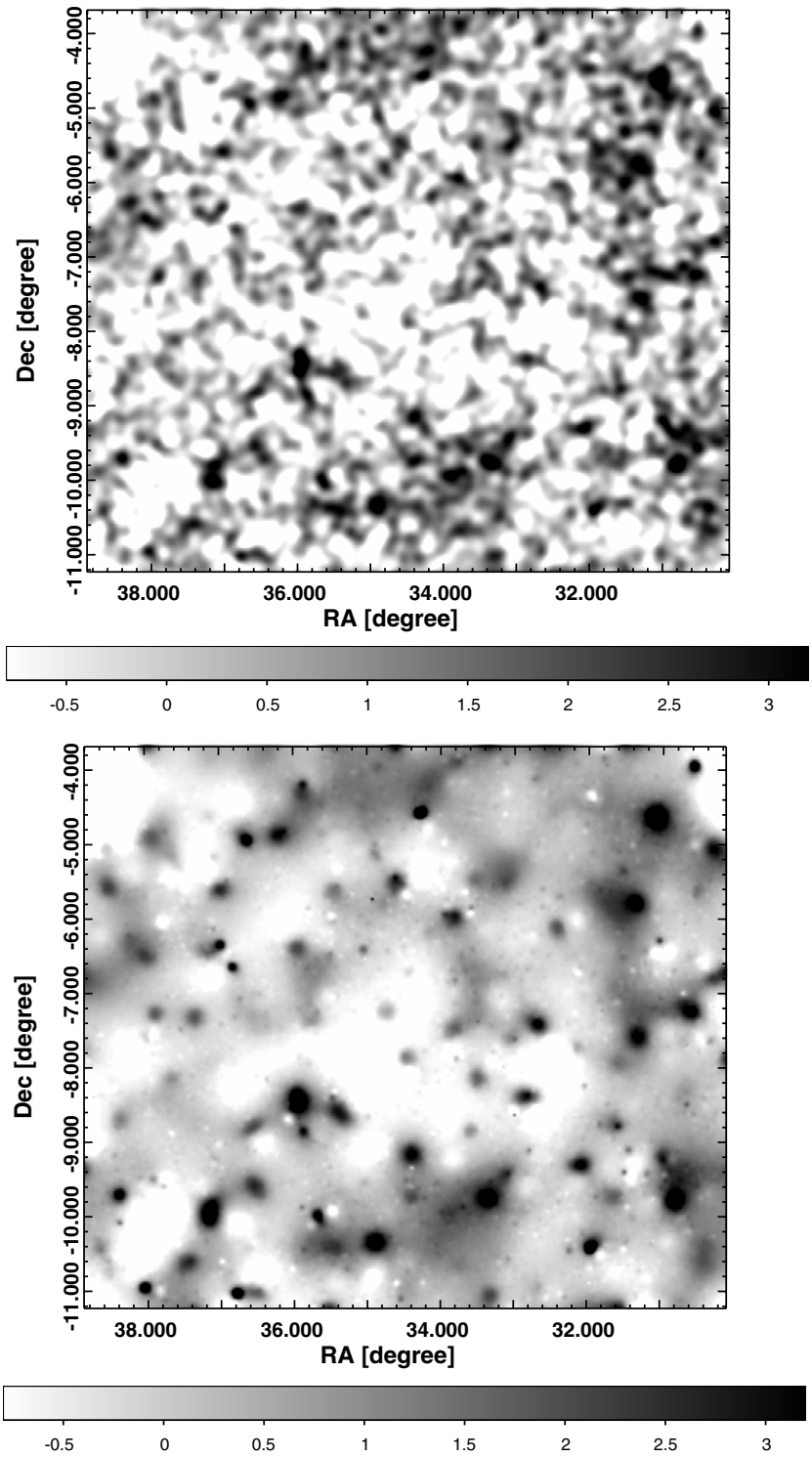

Figure 14. Reconstructed "dark matter mass" convergence map for the entire 64 deg^2 CFHTLS-Wide W1 field showing the same data as Figure 13, but smoothed with a Gaussian filter of width $\theta_G = 6'$ (left) and multi-scale wavelet filtering (right) to highlight the large-scale features.

consistent with analytical predictions within Poisson noise. At very low ν, the number of peaks is washed out and actually decreases when noise is superimposed because it is impossible to extract very low-ν peaks. However, if larger and deeper surveys still find fewer low-ν or high-ν peaks than expected, and systematic effects such as the consequences of masked regions are more fully understood, it may indicate a cosmology with, e.g., lower Ω_m and σ_8 than the values used for our predictions.

Our main conclusions about the distribution of convergence peaks are as follows.

1. Peak counts detected in CFHTLS-Wide are consistent with predictions from a ΛCDM cosmological model once noise effects are properly included (van Waerbeke 2000; Fan et al. 2010).
2. The convergence field is non-Gaussian. The excess of local maxima with $\nu > 3.5$ compared to local minima with

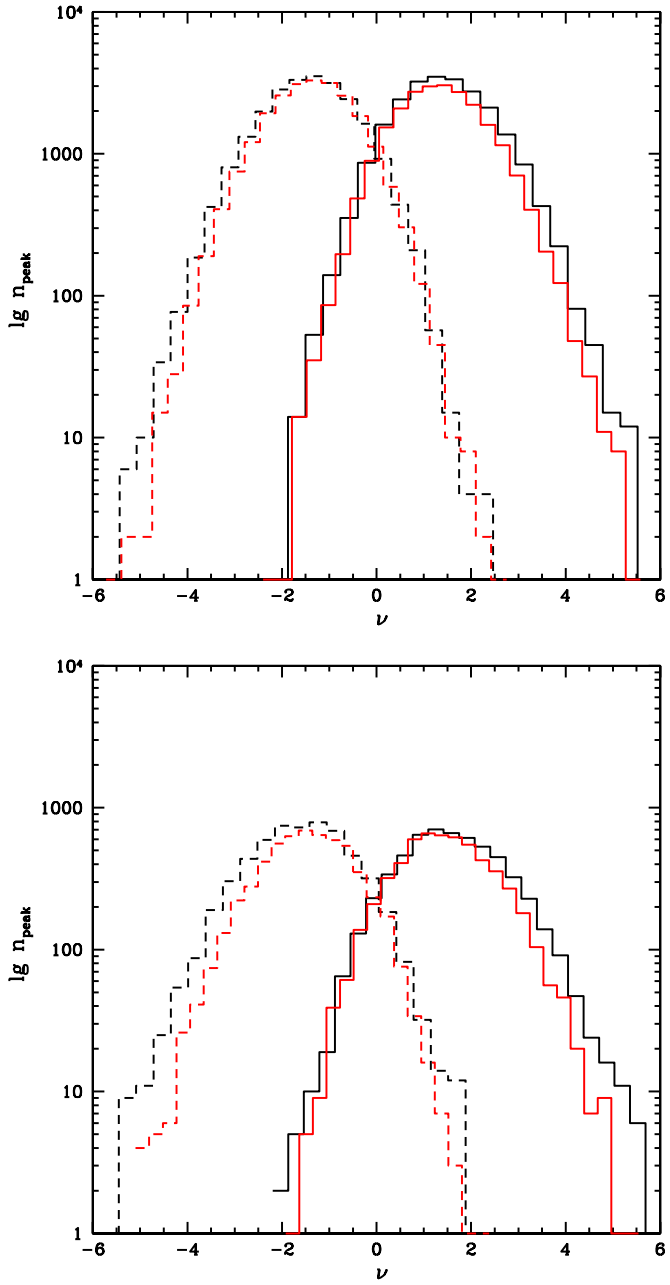

Figure 15. Numbers of local maxima (solid line) and minima (dashed line) in our *E*-mode (black) and *B*-mode (red) convergence map of the CFHTLS-Wide W1 field, with smoothing scales $\theta_G = 1'$ (top-panel) and $\theta_G = 2'$ (bottom-panel). Local maxima can still have a slightly negative peak height if they occur along the same line of sight as a negative noise fluctuation (or a huge void), and local minima can similarly have a slightly positive peak height. To eliminate spurious noise peaks, we shall mainly consider maxima or minima with $|\nu| > 3.5$. In this regime, there is an excess of local maxima over local minima and an excess of *E*-mode peaks over *B*-mode peaks (see Table 2).

(A color version of this figure is available in the online journal.)

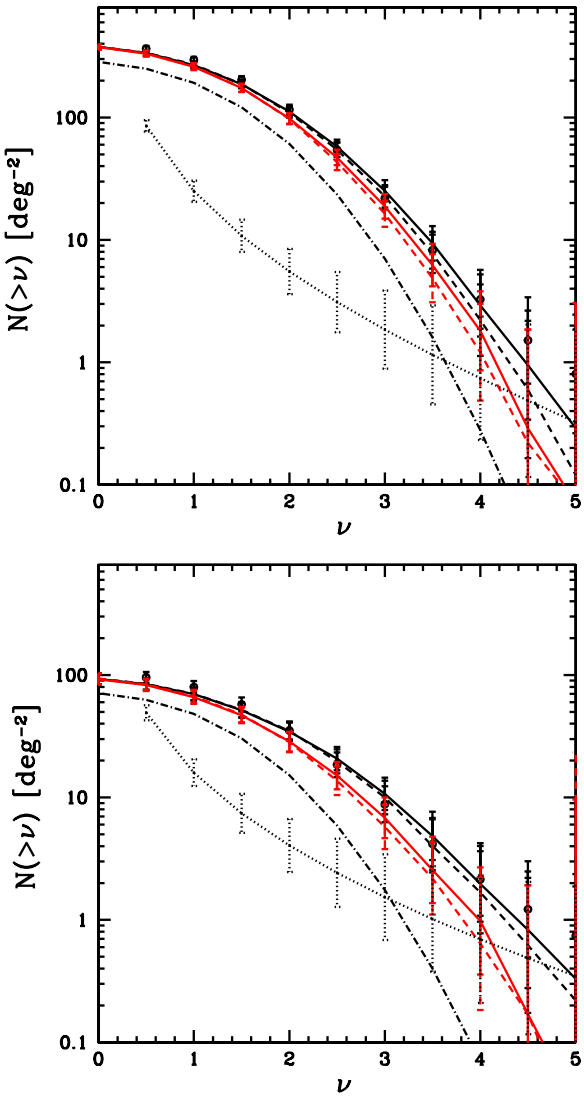

Figure 16. Cumulative density of local maxima $N(> \nu)$ (solid line) and corresponding density of local minima $N(< -\nu)$ (dashed line) in the CFHTLS-Wide W1 *E*-mode (black) and *B*-mode (red) convergence map with smoothing scale $\theta_G = 1'$ (top-panel) and $\theta_G = 2'$ (bottom-panel). Error bars are simply 1σ uncertainties assuming Poisson shot noise. The dot-dashed line shows the prediction from Gaussian random field theory (van Waerbeke 2000). Circles with additional error bars and the dotted curves show an analytical prediction in a ΛCDM universe (Fan et al. 2010), with and without the influence of random noise. The excess of positive maxima over negative minima demonstrates the non-Gaussianity of the convergence field.

(A color version of this figure is available in the online journal.)

$\nu < -3.5$ is also consistent with models (Miyazaki et al. 2002; Gavazzi & Soucail 2007).

3. Noise peaks dominate the expected peak counts due to cosmological weak lensing below $|\nu| \lesssim 3$.

We expect that weak lensing peak counts will become reliably employed to constrain cosmological parameters in future lensing analyses. Although it is difficult to remove the contributions of noise from intrinsic galaxy shapes and the projection of large scale structures, these effects can be analytically predicted. Pushing these predictions into the low signal-to-noise regime might also allow constraints to use a much higher number density of less massive peaks, tightening predictions by reducing Poisson noise.

5. OPTICAL/X-RAY COUNTERPARTS

We shall now compare our weak lensing peak detections with catalogs of overdensities detected via optical or X-ray emission. We adopt the K2 optical cluster catalog constructed using photometric redshifts from the same CFHTLS-Wide W1 imaging (Thanjavur et al. 2009), and the XMM-LSS X-ray selected cluster catalog (Adami et al. 2011), which partially overlaps our survey field.

Table 3
The Detection Purity of Various Weak Lensing Cluster Surveys Described in the Literature

	Weak Lensing Cluster Sample	Comparison Sample	Purity
Hamana et al. (2004)	$n_{\rm gal} = 30$ arcmin^{-2}, $\nu > 4$	Halos (simulations)	60%
Dietrich et al. (2007)	$n_{\rm gal} = 18$ arcmin^{-2},	Halos (simulations)	75%
Miyazaki et al. (2007)	$\nu > 3.69$	X-ray clusters (XMM-LSS)	80%
Gavazzi & Soucail (2007)	$n_{\rm gal} \sim 35$ arcmin^{-2}, $\nu > 3.5$	Photometric clusters	~65%
Schirmer et al. (2007)	$\nu > 4$	BCG	~45%
Geller et al. (2010)	$\nu > 3.5$	Spectroscopic clusters (SHELS)	~33%

Table 4
Cluster Search Purity as a Function of Peak Height Threshold $\nu_{\rm th}$

$\nu_{\rm th}$	$N(\nu > \nu_{\rm th})$	$N_{\rm matched}$ $(\nu > \nu_{\rm th}$, K2)	f_p
3.5	301	126	42%
4.0	125	67	54%
4.5	51	30	59%

We define the purity f_p of our blind weak lensing cluster search as the fraction of peaks above a given detection threshold $\nu_{\rm th}$ that are associated with an optically detected cluster

$$f_p = \frac{N_{\rm matched}(\nu > \nu_{\rm th})}{N(\nu > \nu_{\rm th})}. \quad (15)$$

The expected purity depends upon the survey depth (galaxy density), systematics, and the extent of multi-band or spectroscopic follow-up. Using numerical simulations with $n_{\rm gal} = 30$ arcmin^{-2}, Hamana et al. (2004) predict a purity of more than 60% for convergence peaks with $\nu > 4$. The Bonn Lensing, Optical, and X-ray selected galaxy clusters (*BLOX*) simulations by Dietrich et al. (2007) with $n_{\rm gal} = 18$ arcmin^{-2} also predict that 75% of matches between convergence map peaks and massive halos are within 2.′15. In practice, Miyazaki et al. (2007) achieve 80% purity for the ~100 peaks in Subaru convergence maps with $\nu > 3.69$. Gavazzi & Soucail (2007) obtain ~65% purity from 14 peaks in CFHTLS-Deep with $\nu > 3.5$. Schirmer et al. (2007) obtain ~45% purity for the 158 possible mass concentrations identified in the Garching-Bonn Deep Survey (*GaBoDS*) at $\nu > 4$, consistent with an earlier evaluation of a subsample of the survey (Maturi et al. 2007). Geller et al. (2010) find only ~33% purity by combining the Deep Lens Survey with the Smithsonian Hectospec Lensing Survey (*SHELS*) redshift survey (see Table 3).

Figure 17 shows a subset of our cluster search in the representative W1+2+3 pointing, which also overlaps with the XMM-LSS survey (Pacaud et al. 2007; Adami et al. 2011). The observed weak lensing peak positions may not coincide exactly with cluster centers defined from optical emission because of a combination of noise, substructure, and physical processes associated with cluster mergers (Fan et al. 2010; Hamana et al. 2004). We therefore search for matched pair candidates in K2 within a 3.′0 radius of peaks that appear in both the $\theta_G = 1'$ and $\theta_G = 2'$ lensing map. This search radius is chosen to be larger than the smoothing scale, but smaller than the angular virial radius of a massive cluster at $0.1 < z < 0.9$ (Hamana et al. 2004). If more than one pair exists within 3.′0, we adopt the closest match as the primary candidate.

We obtain 126 matches between weak lensing peaks with $\nu > 3.5$ and optical K2 clusters: corresponding to a purity of 42%. This is lower than in CFHTLS-Deep (Gavazzi & Soucail 2007) because of the much lower source galaxy density. The purity is listed as a function of detection threshold $\nu_{\rm th}$ in Table 4, and the complete catalog of matched pairs is presented in Table 5. Figure 18 shows the separations between the matched weak lensing peaks and K2 centers. The left panel shows the offsets for peaks with $\nu > 0$ in maps with various smoothing scales; the separation between peaks typically matches the smoothing scale. The right panel shows the offsets for only the reliably detected peaks with high ν; the finite number of clusters is too low to draw solid conclusions about the typical separation. Figure 19 shows the redshift distribution of matched clusters relative to the overall K2 sample. Our lensing selection preferentially detects clusters at $0.2 < z < 0.4$ and becomes inefficient above $z > 0.5$.

We also compare our $\nu > 3.5$ lensing peaks with X-ray observations from the XMM-LSS survey. Adami et al. (2011) present 66 spectroscopically confirmed clusters ($0.05 < z < 1.5$) within the 6 deg^2 XMM-LSS survey. This partially overlaps with the CFHTLS-W1 field (53 X-ray clusters are within W1). In this overlap region, we find 31 lensing peaks, 7 of which are within 5.′0 of X-ray clusters. Note that we increase the distance threshold for matches because of additional noise in the X-ray centers and the common phenomenon of separation between the gravitational field and X-ray gas—Shan et al. (2010) found that 45% of a sample of 38 clusters had X-ray offsets >10″. Indeed, in our new sample, we also find that the offsets between weak lensing and X-ray centers are always comparable to or much larger than the offset between weak lensing and optical centers.

Miyazaki et al. (2007) also perform a weak lensing analysis of 0.5 deg^2 of the XMM-LSS survey. They find 15 lensing peaks with optical counterparts, of which 10 match X-ray selected clusters (Adami et al. 2011). Many of the X-ray clusters are simply at too high a redshift to be detected by the CFHTLS lensing data. However, three of these clusters are detected in both our analysis (c77, c92, and c93 in Table 6) and that of Miyazaki et al. (2007).

6. TOMOGRAPHIC ANALYSIS OF LENSING PEAKS

Since multi-band photometric redshift estimates are available for 76% of the source galaxies, we shall now perform a 3D, tomographic shear analysis around all $\nu > 3.5$ cluster candidates with an optical or X-ray counterpart. This process yields an estimate of the cluster redshift (and mass) independently of its visible emission. It also further cleans the cluster catalog of spurious peaks created by either noise or the projection of multiple small systems along a single line of sight.

We fit the 3D shear signal around each cluster candidate to both a singular isothermal sphere (SIS) and a Navarro et al. (1996; NFW) model, with the cluster lens as an additional free parameter. We assume that the center of each cluster candidate is at the position of the brightest central galaxy (BCG). This may not be optimal (Johnston et al. 2007), but it is much more precisely known than the peak of the lensing signal (Fan et al.

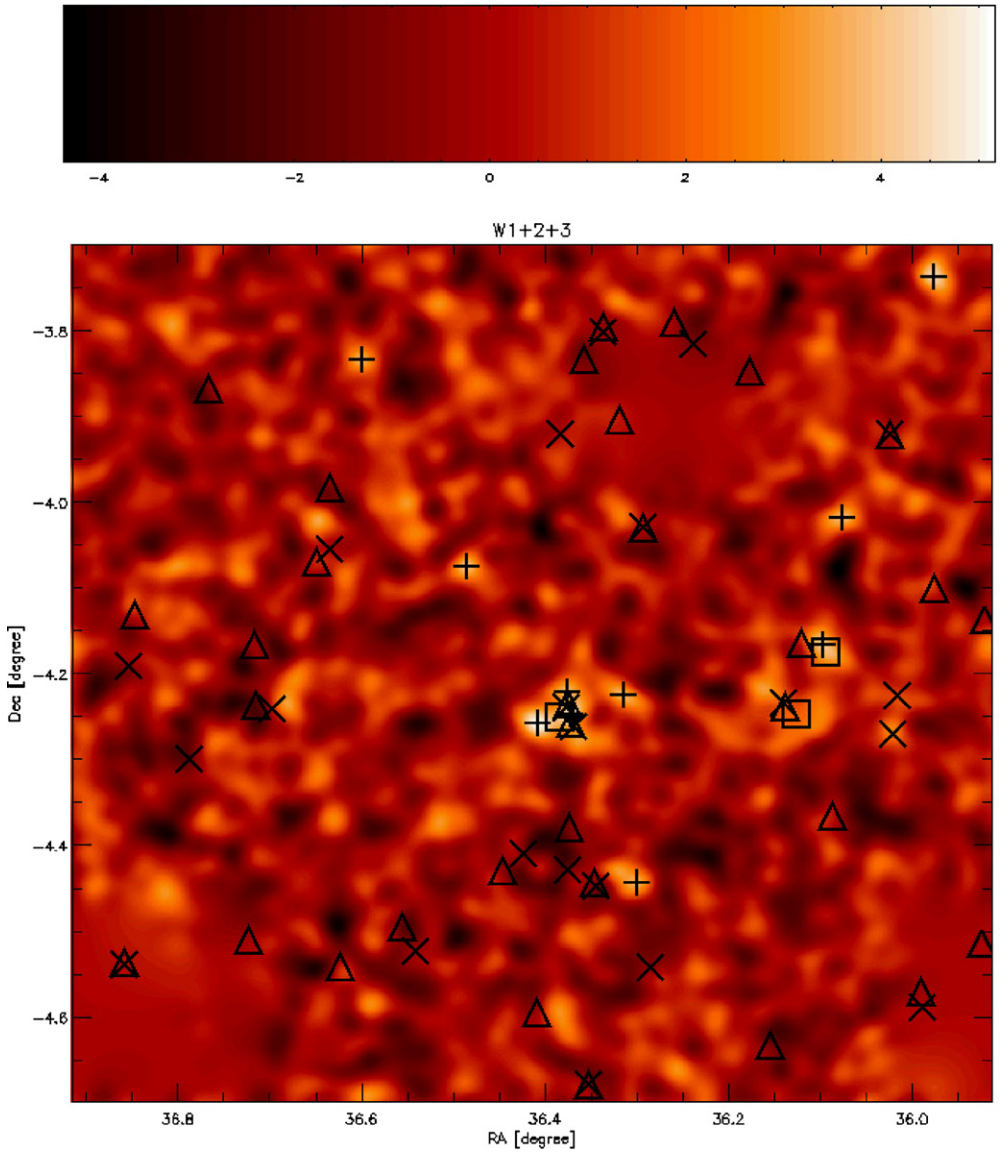

Figure 17. Reconstructed lensing convergence signal-to noise map for the W1+2+3 pointing, plus overlays showing optically and X-ray selected cluster counterparts. The smoothing scale of the background map is $\theta_G = 1'$. Symbols indicate the positions of +: lensing peaks detected with $\nu > 3.5$ in the $\theta_G = 1'$ map, □: lensing peaks detected with $\nu > 3.5$ in the $\theta_G = 2'$ map, △: optically detected clusters in the K2 catalog, and ×: X-ray selected clusters found in XMM-LSS (Adami et al. 2011).

(A color version of this figure is available in the online journal.)

2010). For each source galaxy, we adopt the best-fit redshift from the cleaned Arnouts et al. (2010) catalog. Following Gavazzi & Soucail (2007), we measure the mean tangential shear in a 1′–5′ annulus from the cluster center, excluding the core to minimize dilution of the signal from any cluster member galaxies with incorrect photometric redshifts.

For an SIS model, the component of shear tangential to the cluster center is

$$\gamma_t(\theta, z_s; z_l) = \frac{D_{ls}}{D_s} \frac{4\pi\sigma_v^2}{c^2} \frac{1''}{2\theta}, \tag{16}$$

where θ is the angular distance from the center. We simultaneously fit the unknown lens redshift and characteristic cluster velocity dispersion σ_v by minimizing

$$\chi^2_{\rm SIS}(z_l, \sigma_v) = \sum_i \frac{(\gamma_{t,i} - \gamma_{{\rm SIS},i}(z_l, \sigma_{\rm tomo}))^2}{\sigma^2_{e,i}}, \tag{17}$$

where $w_i = w(z_l, z_{s,i})$ and $\sigma^2_{e,i}$ is given by Equation (2).

The full NFW model has two free parameters, but we assume the Bullock et al. (2001) relation between concentration c and virial mass $M_{\rm vir}$ seen in numerical simulations

$$c_{\rm NFW}(M_{\rm vir}, z) = \frac{c_*}{1+z} \left(\frac{M_{\rm vir}}{10^{14}\, h^{-1}\, M_\odot} \right)^{-0.13}, \tag{18}$$

where $c_* = 8$. As for the SIS model, there is then only one free parameter, and we fit the shear field for lens redshift and halo mass by minimizing

$$\chi^2_{\rm NFW}(z_l, M_{\rm vir}) = \sum_i \frac{(\gamma_{t,i} - \gamma_{\rm NFW}(z_l, M_{\rm vir}))^2}{\sigma^2_{e,i}}. \tag{19}$$

To aid comparison with other work, for each cluster we calculate both the virial mass $M_{\rm vir}$ and the mass M_{200} enclosed within a radius r_{200} in which the mean density of the halo is 200 times the critical density at the redshift of the cluster.

Table 5
Catalog of the Matching Groups/Clusters between $\nu > 3.5$ Convergence Peaks and K2-detected Groups/Clusters in CFHTLS-Wide W1 Fields

ID	z_{K2}	α_{K2}	δ_{K2}	sig_{r-i}	α	δ	d (arcsec)	z_{SIS}	σ_v (km s^{-1})	χ^2_{SIS}	z_{NFW}	m_{NFW} ($10^{14}\,M_\odot\,h^{-1}$)	m_{200} ($10^{14}\,M_\odot\,h^{-1}$)	χ^2_{NFW}	ν
c1-w1	0.18	30.990	−4.223	3.19	30.976	−4.231	59.2	$0.28^{+0.17}_{-0.10}$	$829.7^{+225.1}_{-308.9}$	0.42	$0.29^{+0.16}_{-0.14}$	$2.88^{+6.22}_{-2.15}$	$2.50^{+5.39}_{-1.86}$	0.41	4.458
c2-w1	0.48	30.625	−3.966	4.09	30.619	−3.970	29.6	$0.26^{+0.08}_{-0.10}$	$945.5^{+173.8}_{-212.5}$	1.52	$0.26^{+0.07}_{-0.08}$	$11.0^{+17.8}_{-7.20}$	$9.32^{+15.1}_{-6.10}$	1.50	4.113
c3-w1	0.28	30.421	−5.030	7.45	30.420	−5.030	1.62	$0.26^{+0.11}_{-0.10}$	$701.6^{+134.2}_{-132.8}$	0.85	$0.26^{+0.12}_{-0.12}$	$3.51^{+0.63}_{-0.66}$	$3.02^{+0.54}_{-0.57}$	0.88	5.395
c4-w1	0.72	30.296	−6.089	9.85	30.260	−6.088	128.5	$0.69^{+0.21}_{-0.22}$	∼0	4.33	$0.69^{+0.23}_{-0.20}$	∼0	∼0	4.25	3.732
c5-w1	0.38	30.860	−5.925	4.72	30.867	−5.945	74.3	$0.41^{+0.10}_{-0.09}$	$503.1^{+102.5}_{-104.1}$	1.37	$0.40^{+0.10}_{-0.11}$	$0.78^{+0.16}_{-0.17}$	$0.70^{+0.14}_{-0.15}$	1.37	3.510
c6-w1	0.27	30.840	−7.331	3.68	30.836	−7.341	38.2	$0.20^{+0.09}_{-0.12}$	$559.8^{+131.8}_{-139.6}$	0.68	$0.22^{+0.11}_{-0.10}$	$0.79^{+0.18}_{-0.17}$	$0.69^{+0.16}_{-0.15}$	0.51	4.184
c7-w1	0.33	31.077	−7.213	3.20	31.080	−7.216	15.5	$0.39^{+0.30}_{-0.23}$	$646.1^{+183.9}_{-222.3}$	1.05	$0.40^{+0.25}_{-0.35}$	$1.38^{+2.09}_{-1.18}$	$1.23^{+1.86}_{-1.05}$	1.03	3.677
c8-w1	−99.0	30.779	−7.142	4.28	30.785	−7.141	20.1	$0.76^{+0.15}_{-0.19}$	$162.3^{+137.0}_{-125.4}$	0.78	$0.80^{+0.16}_{-0.17}$	$0.11^{+0.08}_{-0.09}$	$0.10^{+0.07}_{-0.08}$	0.73	4.586
c9-w1	0.81	30.884	−6.736	5.78	30.882	−6.749	46.8	$0.77^{+0.25}_{-0.26}$	$892.1^{+274.1}_{-291.7}$	1.25	$0.78^{+0.24}_{-0.26}$	$4.07^{+0.98}_{-1.04}$	$3.82^{+0.92}_{-0.97}$	1.21	3.722
c10-w1	0.36	30.628	−6.524	5.11	30.649	−6.536	85.3	$0.41^{+0.13}_{-0.12}$	∼0	9.34	$0.41^{+0.12}_{-0.11}$	∼0	∼0	8.30	3.897
c11-w1	0.31	30.364	−8.283	4.20	30.369	−8.275	35.2	$0.35^{+0.16}_{-0.13}$	∼0	5.22	$0.35^{+0.15}_{-0.17}$	∼0	∼0	4.28	3.710
c12-w1	0.14	30.325	−7.651	4.43	30.346	−7.659	81.9	$0.22^{+0.12}_{-0.11}$	$396.6^{+128.6}_{-102.1}$	1.96	$0.42^{+0.15}_{-0.14}$	$0.28^{+0.07}_{-0.06}$	$0.25^{+0.06}_{-0.05}$	1.59	4.728
c13-w1	0.23	30.708	−9.337	4.83	30.704	−9.356	69.7	$0.21^{+0.16}_{-0.10}$	$473.8^{+221.3}_{-239.5}$	2.15	$0.21^{+0.13}_{-0.11}$	$0.16^{+0.08}_{-0.09}$	$0.14^{+0.07}_{-0.08}$	2.01	4.084
c14-w1	0.40	30.534	−8.437	7.52	30.537	−8.417	71.4	$0.43^{+0.09}_{-0.08}$	$691.1^{+102.1}_{-97.8}$	0.14	$0.43^{+0.09}_{-0.11}$	$1.50^{+0.19}_{-0.17}$	$1.34^{+0.17}_{-0.15}$	0.14	4.045
c15-w1	0.32	30.870	−9.817	18.02	30.881	−9.838	86.2	$0.36^{+0.14}_{-0.13}$	$483.9^{+120.9}_{-112.7}$	0.68	$0.36^{+0.13}_{-0.15}$	$0.70^{+0.16}_{-0.18}$	$0.62^{+0.14}_{-0.16}$	0.59	4.835
c16-w1	0.66	30.452	−10.853	5.81	30.463	−10.840	59.6	$0.62^{+0.08}_{-0.09}$	$747.7^{+114.3}_{-117.2}$	1.15	$0.62^{+0.10}_{-0.08}$	$2.24^{+0.33}_{-0.35}$	$2.06^{+0.30}_{-0.32}$	1.07	3.511
c17-w1	0.32	32.021	−4.583	3.85	32.045	−4.542	171.4	$0.35^{+0.10}_{-0.09}$	$931.9^{+218.7}_{-239.2}$	1.12	$0.35^{+0.11}_{-0.14}$	$5.52^{+5.32}_{-3.20}$	$4.81^{+4.63}_{-2.79}$	0.93	3.628
c18-w1	0.25	31.797	−4.002	3.04	31.772	−3.963	165.9	$0.51^{+0.45}_{-0.17}$	$874.1^{+175.9}_{-340.5}$	0.69	$0.50^{+0.21}_{-0.14}$	$5.09^{+6.41}_{-3.42}$	$4.56^{+5.75}_{-3.07}$	0.61	5.011
c19-w1	0.29	31.793	−3.894	4.37	31.792	−3.854	142.4	$0.39^{+0.19}_{-0.18}$	∼0	6.94	$0.38^{+0.20}_{-0.17}$	∼0	∼0	5.82	4.540
c20-w1	0.19	31.283	−4.972	3.17	31.308	−4.993	118.5	$0.12^{+0.12}_{-0.13}$	∼0	5.12	$0.11^{+0.11}_{-0.12}$	∼0	∼0	4.64	3.899
c21-w1	0.42	31.558	−6.167	4.34	31.538	−6.167	70.2	$0.32^{+0.14}_{-0.16}$	∼0	3.73	$0.31^{+0.13}_{-0.11}$	∼0	∼0	4.16	4.142
c22-w1	0.41	31.272	−5.923	4.63	31.254	−5.943	95.4	$0.51^{+0.26}_{-0.25}$	$273.0^{+164.5}_{-157.3}$	1.51	$0.49^{+0.15}_{-0.18}$	$0.24^{+0.16}_{-0.15}$	$0.22^{+0.15}_{-0.14}$	1.22	3.860
c23-w1	0.35	31.667	−7.384	4.89	31.665	−7.400	57.0	$0.26^{+0.21}_{-0.22}$	∼0	3.14	$0.26^{+0.19}_{-0.20}$	∼0	∼0	3.30	4.211
c24-w1	0.40	31.358	−7.588	10.03	31.353	−7.589	20.6	$0.88^{+0.55}_{-0.80}$	$659.3^{+141.3}_{-181.0}$	0.82	$0.88^{+0.11}_{-0.12}$	$1.16^{+0.70}_{-0.45}$	$1.11^{+0.67}_{-0.43}$	0.71	5.311
c25-w1	0.42	31.927	−7.502	3.33	31.953	−7.489	101.7	$0.32^{+0.31}_{-0.28}$	∼0	3.48	$0.32^{+0.29}_{-0.27}$	∼0	∼0	3.48	3.860
c26-w1	0.24	31.320	−7.680	3.00	31.326	−7.664	63.5	$0.22^{+0.13}_{-0.12}$	$417.4^{+138.7}_{-131.5}$	0.86	$0.22^{+0.12}_{-0.12}$	$0.49^{+0.17}_{-0.16}$	$0.43^{+0.15}_{-0.14}$	0.66	4.430
c27-w1	0.26	31.595	−8.807	4.22	31.617	−8.806	75.8	$0.17^{+0.09}_{-0.14}$	$646.2^{+103.0}_{-135.1}$	1.07	$0.19^{+0.11}_{-0.16}$	$1.95^{+1.54}_{-1.27}$	$1.67^{+1.32}_{-1.09}$	1.12	4.423
c28-w1	0.08	31.769	−8.495	3.43	31.724	−8.512	171.6	$0.06^{+0.10}_{-0.11}$	$426.0^{+153.1}_{-166.8}$	2.41	$0.08^{+0.12}_{-0.10}$	$0.65^{+0.21}_{-0.18}$	$0.55^{+0.18}_{-0.15}$	1.54	3.651
c29-w1	0.27	31.230	−10.400	14.90	31.230	−10.407	24.4	$0.21^{+0.16}_{-0.18}$	∼0	5.94	$0.22^{+0.13}_{-0.15}$	∼0	∼0	4.60	4.104
c30-w1	0.19	32.773	−4.129	3.19	32.758	−4.151	96.1	$0.37^{+0.13}_{-0.15}$	$455.5^{+132.6}_{-138.9}$	0.34	$0.40^{+0.14}_{-0.15}$	$0.48^{+0.11}_{-0.13}$	$0.43^{+0.10}_{-0.12}$	0.43	4.674
c31-w1	0.34	32.634	−4.123	6.94	32.653	−4.132	76.5	$0.28^{+0.12}_{-0.11}$	$1134.9^{+243.1}_{-237.0}$	1.38	$0.28^{+0.12}_{-0.12}$	$12.3^{+2.41}_{-2.35}$	$10.5^{+2.05}_{-2.00}$	1.17	4.899
c32-w1	0.28	32.981	−4.688	3.95	32.957	−4.652	157.7	$0.22^{+0.17}_{-0.14}$	∼0	3.59	$0.23^{+0.16}_{-0.17}$	∼0	∼0	3.15	3.737
c33-w1	0.23	32.435	−5.730	3.36	32.456	−5.726	77.9	$0.21^{+0.07}_{-0.10}$	$599.6^{+97.8}_{-117.5}$	1.04	$0.22^{+0.11}_{-0.14}$	$1.09^{+0.12}_{-0.13}$	$0.94^{+0.10}_{-0.11}$	1.11	3.576
c34-w1	0.48	32.669	−7.455	5.61	32.675	−7.449	31.3	$0.36^{+0.14}_{-0.11}$	$703.7^{+150.7}_{-193.7}$	0.73	$0.39^{+0.25}_{-0.17}$	$1.71^{+2.27}_{-1.28}$	$1.52^{+2.02}_{-1.14}$	0.68	4.474
c35-w1	0.45	32.986	−7.123	3.48	32.941	−7.132	163.9	$0.41^{+0.24}_{-0.23}$	$1071.5^{+262.2}_{-239.6}$	1.89	$0.42^{+0.17}_{-0.18}$	$6.89^{+1.07}_{-1.13}$	$6.10^{+0.95}_{-1.00}$	1.81	3.911
c36-w1	0.40	32.865	−6.694	3.31	32.839	−6.726	145.2	$0.36^{+0.15}_{-0.16}$	$580.5^{+121.5}_{-124.3}$	1.51	$0.36^{+0.16}_{-0.17}$	$1.27^{+0.23}_{-0.25}$	$1.13^{+0.20}_{-0.22}$	1.28	4.430
c37-w1	0.62	32.599	−6.543	6.99	32.575	−6.541	85.3	$0.51^{+0.29}_{-0.27}$	∼0	4.12	$0.51^{+0.28}_{-0.27}$	∼0	∼0	4.54	3.504
c38-w1	0.33	32.837	−8.396	8.91	32.824	−8.403	55.2	$0.39^{+0.10}_{-0.10}$	∼0	3.28	$0.41^{+0.11}_{-0.10}$	∼0	∼0	3.17	3.774
c39-w1	0.34	32.135	−7.730	3.54	32.167	−7.750	133.5	$0.37^{+0.17}_{-0.19}$	$682.9^{+225.9}_{-241.1}$	1.34	$0.36^{+0.16}_{-0.18}$	$2.50^{+2.01}_{-1.67}$	$2.19^{+1.76}_{-1.46}$	1.13	3.632
c40-w1	0.46	33.012	−7.676	9.58	33.020	−7.659	69.4	$0.76^{+0.13}_{-0.13}$	$1101.3^{+261.1}_{-263.8}$	1.21	$0.83^{+0.13}_{-0.15}$	$4.49^{+1.18}_{-1.26}$	$4.23^{+1.11}_{-1.19}$	1.05	4.486
c41-w1	0.51	32.658	−7.471	6.09	32.655	−7.445	93.5	$0.55^{+0.21}_{-0.18}$	∼0	4.11	$0.55^{+0.17}_{-0.16}$	∼0	∼0	3.65	4.157
c42-w1	0.71	32.313	−9.244	15.30	32.324	−9.237	44.9	$0.78^{+2.12}_{-0.32}$	$530.9^{+138.9}_{-208.4}$	1.68	$0.77^{+0.13}_{-0.12}$	$1.10^{+0.60}_{-0.40}$	$1.04^{+0.57}_{-0.38}$	1.31	3.792
c43-w1	0.65	32.795	−9.139	6.56	32.815	−9.157	95.8	$0.61^{+0.20}_{-0.12}$	$678.1^{+112.3}_{-143.9}$	0.83	$0.66^{+0.11}_{-0.09}$	$1.80^{+1.15}_{-0.95}$	$1.67^{+1.07}_{-0.88}$	0.66	3.815
c44-w1	0.29	32.553	−8.562	11.58	32.575	−8.560	78.4	$0.25^{+0.12}_{-0.11}$	$971.1^{+342.1}_{-382.5}$	0.74	$0.26^{+0.09}_{-0.08}$	$10.9^{+5.61}_{-6.85}$	$6.85^{+9.30}_{-4.78}$	0.71	4.367
c45-w1	0.30	32.961	−9.994	4.98	32.971	−9.978	68.7	$0.35^{+0.15}_{-0.16}$	∼0	3.51	$0.34^{+0.19}_{-0.17}$	∼0	∼0	3.38	4.109
c46-w1	0.62	32.847	−9.875	3.04	32.883	−9.877	129.3	$0.67^{+0.17}_{-0.16}$	$521.8^{+133.9}_{-129.1}$	1.67	$0.67^{+0.16}_{-0.18}$	$0.66^{+0.12}_{-0.14}$	$0.62^{+0.11}_{-0.13}$	1.56	4.238
c47-w1	0.28	33.607	−6.461	9.74	33.596	−6.454	47.5	$0.24^{+0.11}_{-0.10}$	$698.8^{+198.2}_{-211.7}$	1.41	$0.25^{+0.10}_{-0.10}$	$2.35^{+1.12}_{-1.09}$	$2.04^{+0.97}_{-0.95}$	1.28	3.562
c48-w1	0.65	34.017	−6.137	11.48	34.001	−6.095	161.7	$0.64^{+0.29}_{-0.14}$	$152.8^{+162.4}_{-139.6}$	0.65	$0.64^{+0.19}_{-0.15}$	$0.07^{+0.11}_{-0.10}$	$0.06^{+0.10}_{-0.09}$	0.63	3.930
c49-w1	0.30	33.780	−5.981	7.22	33.779	−5.978	11.9	$0.25^{+0.13}_{-0.13}$	$547.5^{+120.8}_{-117.9}$	2.59	$0.27^{+0.14}_{-0.11}$	$0.78^{+0.18}_{-0.16}$	$0.69^{+0.16}_{-0.14}$	1.83	4.728
c50-w1	0.19	33.941	−5.930	3.46	33.956	−5.976	174.8	$0.37^{+0.16}_{-0.17}$	$667.4^{+156.3}_{-198.7}$	1.28	$0.37^{+0.12}_{-0.14}$	$2.49^{+2.22}_{-1.55}$	$2.20^{+1.96}_{-1.37}$	1.18	3.579
c51-w1	0.35	33.293	−5.625	4.20	33.295	−5.613	40.8	$0.25^{+0.07}_{-0.10}$	$629.1^{+98.4}_{-118.7}$	1.96	$0.25^{+0.11}_{-0.13}$	$1.86^{+2.20}_{-1.44}$	$1.61^{+1.90}_{-1.25}$	1.70	4.205

Table 5
(Continued)

ID	z_{K2}	α_{K2}	δ_{K2}	sig_{r-i}	α	δ	d (arcsec)	z_{SIS}	σ_v (km s^{-1})	χ^2_{SIS}	z_{NFW}	m_{NFW} ($10^{14}\,M_\odot\,h^{-1}$)	m_{200} ($10^{14}\,M_\odot\,h^{-1}$)	χ^2_{NFW}	ν
c52-w1	0.69	33.528	−7.145	5.13	33.509	−7.148	67.8	$0.31^{+0.29}_{-0.30}$	∼0	7.76	$0.33^{+0.21}_{-0.22}$	∼0	∼0	6.81	3.739
c53-w1	0.28	33.402	−6.953	3.15	33.384	−6.944	70.6	$0.23^{+0.12}_{-0.11}$	$694.7^{+133.5}_{-129.8}$	0.86	$0.22^{+0.11}_{-0.11}$	$1.65^{+0.29}_{-0.21}$	$1.44^{+0.25}_{-0.18}$	0.61	4.166
c54-w1	0.31	33.728	−6.539	4.65	33.748	−6.495	171.4	$0.38^{+0.14}_{-0.15}$	$193.1^{+109.6}_{-101.3}$	1.77	$0.37^{+0.16}_{-0.14}$	$0.19^{+0.10}_{-0.11}$	$0.17^{+0.09}_{-0.10}$	1.73	3.590
c55-w1	0.32	33.113	−9.926	9.79	33.130	−9.950	106.0	$0.83^{+2.07}_{-0.30}$	$606.1^{+163.2}_{-231.8}$	1.63	$0.84^{+0.14}_{-0.13}$	$0.97^{+0.33}_{-0.29}$	$0.92^{+0.31}_{-0.28}$	1.58	3.809
c56-w1	0.34	33.720	−9.936	3.35	33.737	−9.908	118.3	$0.50^{+0.21}_{-0.19}$	$597.4^{+147.1}_{-138.2}$	0.93	$0.49^{+0.19}_{-0.19}$	$1.09^{+0.19}_{-0.20}$	$0.99^{+0.17}_{-0.18}$	0.94	3.872
c57-w1	0.39	33.427	−9.769	4.34	33.426	−9.770	4.689	$0.42^{+0.15}_{-0.14}$	$514.7^{+128.7}_{-123.5}$	0.16	$0.43^{+0.13}_{-0.15}$	$0.74^{+0.16}_{-0.18}$	$0.66^{+0.14}_{-0.16}$	0.16	3.570
c58-w1	0.51	34.244	−4.554	6.43	34.233	−4.585	118.0	$0.56^{+0.25}_{-0.16}$	$449.3^{+211.9}_{-163.0}$	1.34	$0.55^{+0.21}_{-0.18}$	$0.45^{+0.20}_{-0.14}$	$0.42^{+0.18}_{-0.13}$	1.21	6.448
c59-w1	0.75	34.071	−4.157	9.06	34.030	−4.131	174.9	$0.82^{+0.22}_{-0.23}$	∼0	3.87	$0.85^{+0.21}_{-0.21}$	∼0	∼0	3.70	3.564
c60-w1	0.62	34.400	−3.946	13.75	34.436	−3.978	176.1	$0.65^{+0.19}_{-0.17}$	$830.3^{+196.8}_{-225.4}$	1.32	$0.64^{+0.16}_{-0.17}$	$4.63^{+1.15}_{-1.17}$	$4.24^{+1.05}_{-1.07}$	1.23	4.363
c61-w1	0.37	34.327	−3.772	3.13	34.311	−3.749	100.0	$0.27^{+0.12}_{-0.14}$	∼0	3.56	$0.29^{+0.13}_{-0.12}$	∼0	∼0	3.21	3.791
c62-w1	0.36	34.657	−5.570	4.17	34.684	−5.572	98.4	$0.57^{+0.13}_{-0.14}$	$909.7^{+61.5}_{-60.1}$	1.55	$0.55^{+0.15}_{-0.13}$	$5.31^{+0.32}_{-0.30}$	$4.82^{+0.29}_{-0.27}$	1.47	4.194
c63-w1	0.79	34.511	−6.743	15.30	34.531	−6.488	89.8	$0.70^{+0.31}_{-0.28}$	∼0	4.33	$0.71^{+0.26}_{-0.25}$	∼0	∼0	4.09	3.931
c64-w1	0.33	34.655	−5.674	9.59	34.653	−5.626	170.7	$0.42^{+0.14}_{-0.11}$	∼0	4.18	$0.41^{+0.13}_{-0.10}$	∼0	∼0	3.87	4.186
c65-w1	0.35	34.092	−7.369	5.17	34.070	−7.380	87.7	$0.27^{+0.12}_{-0.12}$	∼0	4.28	$0.26^{+0.10}_{-0.09}$	∼0	∼0	4.09	5.230
c66-w1	0.33	34.483	−6.755	3.35	34.449	−6.742	129.5	$0.31^{+0.10}_{-0.19}$	∼0	3.26	$0.31^{+0.11}_{-0.10}$	∼0	∼0	3.13	4.692
c67-w1	0.22	34.350	−6.687	3.84	34.390	−6.717	180.0	$0.37^{+0.26}_{-0.19}$	$794.7^{+235.7}_{-340.1}$	1.72	$0.39^{+0.06}_{-0.05}$	$3.63^{+0.90}_{-1.71}$	$3.20^{+0.79}_{-1.51}$	1.51	4.515
c68-w1	0.33	34.219	−8.229	7.14	34.219	−8.223	21.6	$0.38^{+0.16}_{-0.17}$	∼0	3.09	$0.37^{+0.15}_{-0.16}$	∼0	∼0	3.06	3.967
c69-w1	0.71	34.948	−8.120	13.80	34.965	−8.091	117.5	$0.75^{+0.21}_{-0.18}$	$514.0^{+123.4}_{-109.9}$	1.27	$0.74^{+0.19}_{-0.18}$	$0.63^{+0.15}_{-0.14}$	$0.59^{+0.14}_{-0.13}$	1.22	3.737
c70-w1	0.70	34.837	−7.585	13.38	34.829	−7.570	59.7	$0.76^{+0.07}_{-0.08}$	$545.4^{+94.2}_{-98.4}$	0.62	$0.76^{+0.06}_{-0.08}$	$0.90^{+0.13}_{-0.17}$	$0.85^{+0.12}_{-0.16}$	0.58	4.497
c71-w1	0.28	34.415	−9.099	6.19	34.419	−9.104	21.4	$0.43^{+0.05}_{-0.06}$	$1342.7^{+242.7}_{-249.2}$	0.95	$0.44^{+0.06}_{-0.06}$	$33.1^{+5.21}_{-5.32}$	$28.7^{+4.51}_{-4.61}$	0.85	5.520
c72-w1	0.31	34.476	−9.849	4.14	34.439	−9.837	138.6	$0.31^{+0.13}_{-0.14}$	$1079.6^{+251.6}_{-266.8}$	1.24	$0.27^{+0.16}_{-0.14}$	$13.2^{+2.86}_{-2.73}$	$11.3^{+2.44}_{-2.33}$	1.23	3.705
c73-w1	0.32	34.692	−9.463	3.50	34.729	−9.454	132.6	$0.22^{+0.11}_{-0.15}$	∼0	3.61	$0.22^{+0.13}_{-0.15}$	∼0	∼0	3.58	3.800
c74-w1	0.41	34.280	−9.354	15.23	34.290	−9.367	60.1	$0.47^{+0.17}_{-0.18}$	∼0	3.33	$0.49^{+0.16}_{-0.17}$	∼0	∼0	3.30	3.990
c75-w1	0.21	34.029	−10.419	3.37	34.055	−10.421	92.8	$0.53^{+0.97}_{-0.17}$	$506.9^{+140.8}_{-207.8}$	1.45	$0.57^{+0.92}_{-0.18}$	$0.57^{+0.82}_{-0.45}$	$0.53^{+0.76}_{-0.42}$	1.42	4.841
c76-w1	−99.0	35.401	−4.420	3.72	35.374	−4.391	140.7	$0.50^{+0.23}_{-0.25}$	∼0	6.14	$0.42^{+0.23}_{-0.21}$	∼0	∼0	5.80	4.355
c77-w1	0.43	35.441	−3.772	22.39	35.456	−3.768	57.2	$0.34^{+0.11}_{-0.12}$	$766.1^{+182.5}_{-229.9}$	0.86	$0.35^{+0.15}_{-0.15}$	$2.04^{+2.78}_{-1.54}$	$1.79^{+2.44}_{-1.35}$	0.82	4.209
c78-w1	0.44	35.595	−4.890	3.26	35.601	−4.892	23.0	$0.31^{+0.15}_{-0.13}$	∼0	4.45	$0.31^{+0.14}_{-0.15}$	∼0	∼0	4.17	3.788
c79-w1	0.04	35.216	−4.782	3.08	35.229	−4.743	150.3	$0.06^{+0.12}_{-0.11}$	$573.8^{+113.9}_{-108.7}$	1.16	$0.07^{+0.11}_{-0.10}$	$2.78^{+0.33}_{-0.31}$	$2.30^{+0.27}_{-0.26}$	1.09	4.204
c80-w1	0.59	35.436	−6.358	6.80	35.436	−6.354	14.1	$0.45^{+0.19}_{-0.17}$	∼0	6.63	$0.43^{+0.20}_{-0.19}$	∼0	∼0	5.90	4.710
c81-w1	0.22	35.590	−5.682	3.09	35.569	−5.723	164.9	$0.59^{+0.11}_{-0.12}$	$1266.7^{+108.9}_{-117.3}$	1.35	$0.67^{+0.13}_{-0.11}$	$10.9^{+1.70}_{-1.50}$	$9.97^{+1.56}_{-1.37}$	1.29	4.870
c82-w1	0.37	35.650	−7.270	3.34	35.680	−7.281	112.4	$0.32^{+0.13}_{-0.11}$	$628.4^{+106.1}_{-104.6}$	1.22	$0.33^{+0.12}_{-0.10}$	$1.80^{+0.22}_{-0.25}$	$1.59^{+0.19}_{-0.22}$	1.21	3.923
c83-w1	0.32	35.830	−7.997	5.21	35.826	−7.992	21.4	$0.08^{+0.07}_{-0.09}$	$954.6^{120.0}_{132.6}$	1.68	$0.10^{+0.04}_{-0.05}$	$11.1^{+1.26}_{-1.30}$	$9.10^{+1.03}_{-1.07}$	1.67	4.287
c84-w1	0.02	35.924	−7.989	3.40	35.931	−7.994	31.5	$0.16^{+0.04}_{-0.05}$	$789.9^{+64.3}_{-69.1}$	0.15	$0.12^{+0.02}_{-0.01}$	$7.50^{+0.82}_{-0.77}$	$6.21^{+0.68}_{-0.64}$	0.19	4.127
c85-w1	0.35	35.486	−8.950	7.92	35.486	−8.937	48.4	$0.25^{+0.15}_{-0.18}$	∼0	3.98	$0.24^{+0.17}_{-0.19}$	∼0	∼0	3.91	4.372
c86-w1	0.27	35.868	−8.865	5.82	35.883	−8.864	55.4	$0.34^{+0.16}_{-0.14}$	$523.9^{+122.8}_{-118.9}$	0.65	$0.36^{+0.15}_{-0.16}$	$0.79^{+0.12}_{-0.13}$	$0.70^{+0.11}_{-0.12}$	0.41	4.779
c87-w1	0.32	35.821	−9.347	6.25	35.805	−9.344	61.1	$0.38^{+0.19}_{-0.22}$	∼0	3.52	$0.39^{+0.18}_{-0.20}$	∼0	∼0	2.94	3.690
c88-w1	0.24	35.941	−10.924	5.53	35.935	−10.888	129.8	$0.26^{+0.08}_{-0.09}$	$538.0^{+112.3}_{-107.2}$	0.27	$0.25^{+0.10}_{-0.08}$	$0.90^{+0.15}_{-0.16}$	$0.78^{+0.13}_{-0.14}$	0.22	3.543
c89-w1	0.34	35.827	−10.399	3.79	35.828	−10.406	26.4	$0.43^{+0.17}_{-0.12}$	∼0	4.77	$0.42^{+0.16}_{-0.13}$	∼0	∼0	3.70	5.260
c90-w1	0.19	35.520	−10.346	4.55	35.488	−10.353	118.1	$0.08^{+0.11}_{-0.10}$	∼0	2.96	$0.10^{+0.12}_{-0.10}$	∼0	∼0	3.11	3.640
c91-w1	0.20	35.284	−10.330	4.14	35.317	−10.305	149.6	$0.28^{+0.13}_{-0.14}$	∼0	4.19	$0.26^{+0.14}_{-0.12}$	∼0	∼0	3.72	4.422
c92-w1	0.65	36.372	−4.258	4.79	36.372	−4.248	36.9	$0.65^{+0.26}_{-0.26}$	∼0	5.69	$0.66^{+0.22}_{-0.20}$	∼0	∼0	4.63	4.548
c93-w1	0.30	36.121	−4.165	3.36	36.097	−4.167	87.5	$0.26^{+0.13}_{-0.12}$	$359.6^{+131.2}_{-121.7}$	0.25	$0.25^{+0.11}_{-0.11}$	$0.77^{+0.17}_{-0.18}$	$0.67^{+0.15}_{-0.16}$	0.20	4.063
c94-w1	0.55	36.108	−5.088	3.13	36.077	−5.102	122.2	$0.20^{+0.17}_{-0.15}$	$344.8^{+97.5}_{-89.1}$	0.78	$0.20^{+0.18}_{-0.16}$	$0.23^{+0.06}_{-0.04}$	$0.20^{+0.05}_{-0.04}$	0.81	3.521
c95-w1	0.35	36.617	−4.998	10.12	36.636	−4.990	72.8	$0.22^{+0.14}_{-0.15}$	∼0	4.55	$0.21^{+0.13}_{-0.14}$	∼0	∼0	4.15	3.948
c96-w1	0.50	36.121	−4.821	8.92	36.116	−4.852	114.5	$0.47^{+0.12}_{-0.14}$	$701.3^{+131.3}_{-129.0}$	0.61	$0.47^{+0.13}_{-0.12}$	$2.10^{+0.31}_{-0.27}$	$1.89^{+0.28}_{-0.24}$	0.57	4.211
c97-w1	0.29	36.455	−5.896	10.48	36.465	−5.892	38.6	$0.35^{+0.11}_{-0.12}$	$430.4^{+116.3}_{-120.2}$	0.79	$0.35^{+0.13}_{-0.12}$	$0.53^{+0.12}_{-0.11}$	$0.47^{+0.11}_{-0.10}$	0.76	4.505
c98-w1	0.32	36.631	−5.695	3.81	36.635	−5.692	17.3	$0.23^{+0.10}_{-0.11}$	∼0	4.40	$0.24^{+0.12}_{-0.15}$	∼0	∼0	4.36	4.147
c99-w1	0.51	36.890	−7.462	3.34	36.903	−7.483	88.4	$0.48^{+0.13}_{-0.19}$	$1055.6^{+263.4}_{-305.1}$	1.73	$0.49^{+0.14}_{-0.18}$	$6.03^{+1.27}_{-1.32}$	$5.41^{+1.14}_{-1.18}$	1.51	3.546
c100-w1	0.31	35.996	−8.595	18.74	36.008	−8.599	45.3	$0.36^{+0.16}_{-0.14}$	$905.3^{+182.9}_{-193.5}$	0.87	$0.35^{+0.15}_{-0.16}$	$4.53^{+0.85}_{-0.91}$	$3.92^{+0.74}_{-0.79}$	0.73	4.631
c101-w1	0.34	36.405	−9.775	5.22	36.415	−9.758	72.7	$0.30^{+0.09}_{-0.07}$	$670.8^{+103.7}_{-92.8}$	1.36	$0.31^{+0.07}_{-0.06}$	$1.26^{+0.19}_{-0.22}$	$1.11^{+0.17}_{-0.19}$	1.23	3.856
c102-w1	0.33	36.402	−11.158	6.97	36.398	−11.166	30.2	$0.24^{+0.11}_{-0.19}$	∼0	2.95	$0.27^{+0.12}_{-0.11}$	∼0	∼0	3.08	4.075
c103-w1	0.27	36.785	−11.058	4.54	36.791	−11.053	27.7	$0.29^{+0.12}_{-0.15}$	$301.5^{+152.2}_{-158.7}$	0.59	$0.29^{+0.14}_{-0.13}$	$0.15^{+0.09}_{-0.11}$	$0.13^{+0.08}_{-0.10}$	0.50	3.725

Table 5
(Continued)

ID	z_{K2}	α_{K2}	δ_{K2}	sig_{r-i}	α	δ	d (arcsec)	z_{SIS}	σ_v (km s^{-1})	χ^2_{SIS}	z_{NFW}	m_{NFW} ($10^{14}\,M_\odot\,h^{-1}$)	m_{200} ($10^{14}\,M_\odot\,h^{-1}$)	χ^2_{NFW}	ν
c104-w1	0.29	36.473	−10.992	3.88	36.476	−10.988	15.2	$0.23^{+0.05}_{-0.05}$	$1567.2^{+188.5}_{-185.9}$	0.96	$0.24^{+0.06}_{-0.05}$	$46.6^{+3.32}_{-2.45}$	$38.9^{+2.77}_{-2.04}$	0.90	3.838
c105-w1	0.29	37.199	−5.589	6.37	37.200	−5.618	103.7	$0.32^{+0.07}_{-0.08}$	$729.8^{+93.6}_{-89.8}$	0.19	$0.33^{+0.08}_{-0.08}$	$3.43^{+0.31}_{-0.22}$	$2.97^{+0.27}_{-0.19}$	0.18	3.713
c106-w1	0.32	37.662	−4.991	10.71	37.670	−4.988	36.7	$0.79^{+3.20}_{-0.26}$	$700.2^{+231.9}_{-322.5}$	1.53	$0.75^{+1.23}_{-0.22}$	$1.77^{+2.77}_{-1.56}$	$1.66^{+2.60}_{-1.47}$	1.60	4.449
c107-w1	0.34	37.720	−4.855	7.63	37.724	−4.863	30.6	$0.27^{+0.08}_{-0.06}$	$324.6^{+92.8}_{-83.7}$	0.69	$0.26^{+0.08}_{-0.07}$	$0.26^{+0.10}_{-0.11}$	$0.23^{+0.09}_{-0.10}$	0.62	4.784
c108-w1	0.30	37.358	−4.816	3.08	37.359	−4.835	71.2	$0.33^{+0.13}_{-0.09}$	$348.6^{+113.3}_{-104.2}$	0.56	$0.33^{+0.12}_{-0.10}$	$0.24^{+0.07}_{-0.09}$	$0.21^{+0.06}_{-0.08}$	0.53	3.655
c109-w1	−99.0	37.000	−6.397	3.17	37.022	−6.429	117.5	$0.46^{+0.16}_{-0.09}$	$741.4^{+152.6}_{-194.8}$	1.72	$0.43^{+0.16}_{-0.11}$	$3.17^{+3.32}_{-2.07}$	$2.82^{+2.95}_{-1.84}$	1.25	3.946
c110-w1	0.49	37.812	−5.572	3.10	37.784	−5.587	116.9	$0.52^{+0.17}_{-0.15}$	$303.5^{+141.2}_{-133.1}$	0.89	$0.52^{+0.15}_{-0.13}$	$0.16^{+0.10}_{-0.07}$	$0.15^{+0.09}_{-0.06}$	0.83	4.335
c111-w1	0.28	37.767	−7.269	10.60	37.776	−7.272	33.9	$0.37^{+0.12}_{-0.10}$	∼0	3.17	$0.36^{+0.11}_{-0.11}$	∼0	∼0	3.18	3.708
c112-w1	0.36	37.541	−7.536	3.04	37.540	−7.513	81.0	$0.42^{+0.16}_{-0.18}$	$817.2^{+164.2}_{-177.0}$	0.87	$0.43^{+0.17}_{-0.17}$	$3.76^{+0.72}_{-0.74}$	$3.34^{+0.64}_{-0.66}$	0.81	4.646
c113-w1	0.19	37.354	−7.494	5.18	37.340	−7.486	58.8	$0.39^{+0.09}_{-0.10}$	∼0	4.83	$0.38^{+0.10}_{-0.10}$	∼0	∼0	4.41	3.725
c114-w1	0.37	37.088	−9.226	3.35	37.096	−9.242	62.4	$0.35^{+0.11}_{-0.13}$	$672.0^{+114.3}_{-119.5}$	1.21	$0.35^{+0.12}_{-0.13}$	$2.71^{+0.56}_{-0.51}$	$2.39^{+0.49}_{-0.45}$	1.10	3.616
c115-w1	0.27	37.299	−8.901	3.48	37.294	−8.892	35.3	$0.31^{+0.12}_{-0.14}$	$947.2^{+155.7}_{-168.3}$	2.47	$0.32^{+0.13}_{-0.14}$	$5.55^{+0.72}_{-0.75}$	$4.77^{+0.62}_{-0.64}$	2.44	4.734
c116-w1	0.28	37.355	−8.841	5.10	37.347	−8.835	34.1	$0.26^{+0.16}_{-0.15}$	$174.9^{+194.5}_{-189.3}$	2.81	$0.25^{+0.16}_{-0.17}$	$0.08^{+0.13}_{-0.14}$	$0.07^{+0.12}_{-0.13}$	2.67	4.513
c117-w1	0.64	37.828	−11.147	5.49	37.802	−11.140	93.2	$0.77^{+0.27}_{-0.25}$	∼0	5.64	$0.74^{+0.24}_{-0.25}$	∼0	∼0	5.46	3.684
c118-w1	0.27	37.922	−4.883	12.07	37.936	−4.880	54.2	$0.29^{+0.13}_{-0.12}$	$311.2^{+103.4}_{-97.4}$	0.56	$0.30^{+0.11}_{-0.12}$	$0.14^{+0.05}_{-0.06}$	$0.12^{+0.04}_{-0.05}$	0.53	3.555
c119-w1	0.49	38.525	−4.728	3.14	38.483	−4.737	153.6	$0.46^{+0.14}_{-0.11}$	$422.1^{+126.1}_{-135.6}$	0.48	$0.46^{+0.13}_{-0.14}$	$0.24^{+0.11}_{-0.08}$	$0.22^{+0.10}_{-0.07}$	0.43	3.567
c120-w1	0.31	38.048	−6.491	5.70	38.022	−6.501	102.0	$0.12^{+0.11}_{-0.12}$	∼0	3.77	$0.16^{+0.12}_{-0.11}$	∼0	∼0	3.71	3.850
c121-w1	0.33	37.925	−7.790	3.65	37.938	−7.828	145.0	$0.37^{+0.12}_{-0.11}$	$725.9^{+152.9}_{-143.8}$	0.16	$0.37^{+0.14}_{-0.12}$	$2.12^{+0.39}_{-0.43}$	$1.86^{+0.34}_{-0.38}$	0.16	3.853
c122-w1	0.43	37.998	−7.624	3.44	37.986	−7.658	130.0	$0.33^{+0.15}_{-0.17}$	∼0	3.83	$0.32^{+0.16}_{-0.15}$	∼0	∼0	3.74	3.725
c123-w1	0.37	38.688	−8.801	3.62	38.737	−8.797	172.1	$0.41^{+0.13}_{-0.13}$	$547.5^{+117.8}_{-102.7}$	1.19	$0.40^{+0.12}_{-0.13}$	$1.81^{+0.29}_{-0.31}$	$1.60^{+0.26}_{-0.27}$	1.13	3.563
c124-w1	0.23	38.669	−9.835	3.70	38.630	−9.843	141.1	$0.26^{+0.15}_{-0.15}$	$756.0^{+143.0}_{-139.6}$	0.57	$0.26^{+0.15}_{-0.14}$	$7.14^{+1.32}_{-1.27}$	$6.09^{+1.13}_{-1.08}$	0.56	4.467
c125-w1	0.63	37.902	−9.562	4.82	37.907	−9.595	117.5	$0.59^{+0.29}_{-0.18}$	$814.3^{+313.2}_{-187.3}$	1.53	$0.57^{+0.33}_{-0.15}$	$3.00^{+3.14}_{-1.90}$	$2.74^{+2.86}_{-1.73}$	1.47	4.915
c126-w1	0.26	38.639	−10.472	5.31	38.647	−10.458	57.3	$0.44^{+0.10}_{-0.10}$	$536.5^{+102.1}_{-108.7}$	1.62	$0.40^{+0.11}_{-0.10}$	$0.96^{+0.15}_{-0.13}$	$0.86^{+0.13}_{-0.12}$	1.16	4.764

Note. K2 redshift denotes the median redshift of bright ($i \leqslant 20$) cluster members.

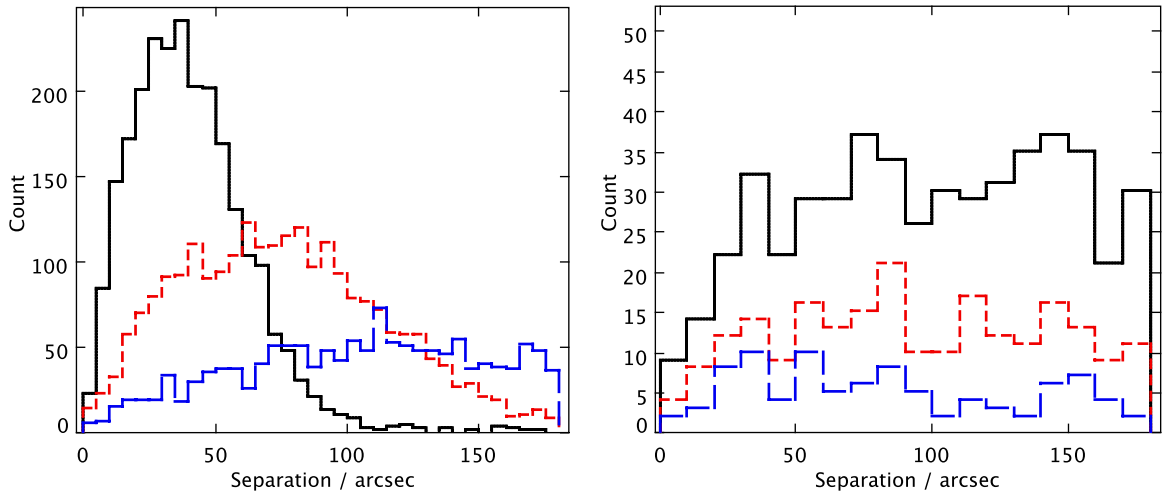

Figure 18. Distribution of the offsets between matched pairs of weak lensing peaks and K2-detected clusters. Left: offsets for all peaks in maps with smoothing scales of 0.′5 (solid black), 1′ (dotted red), and 2′ (dashed blue). Right: offsets for peaks with $\nu > 3$ (solid black histograms), $\nu > 3.5$ (dotted red histograms), and $\nu > 4$ (dashed blue histograms), all with the smoothing scale $\theta = 1$ arcmin.

(A color version of this figure is available in the online journal.)

Figure 20 illustrates our 3D tomographic results on one cluster (identification c3). The mean tangential shear is consistent with zero for $z_s \leqslant 0.26$. The subsequent increase with redshift is clear and allows for an unambiguous identification of the lens redshift. Error bars are derived from the scatter in observed ellipticities (intrinsic+measurement error), as determined by Equation (1). The observed tangential shear profile is consistent with either an SIS or NFW model. Due to our low density of source galaxies and our exclusion of galaxies within the central 1′, we have insufficient signal-to-noise for individual clusters to distinguish between the two models, which differ most noticeably near the core. The amplitude of the systematic B-mode signal, computed by rotating all shear estimates by 45°, is always at least one order of magnitude smaller than the tangential shear, and it oscillates about zero.

Figure 21 shows the signal-to-noise contours of the convergence signal reconstructed around four clusters from the 3D shear signal.

Table 6
Catalog of the Matching Groups/Clusters between $\nu > 3.5$ Convergence Peaks and X-Ray/K2-detected Groups/Clusters in CFHTLS-Wide W1 Fields

ID	$\alpha_{\rm xray}$	$\delta_{\rm xray}$	$\alpha_{\rm K2}$	$\delta_{\rm K2}$	α	δ	$d_{\rm xray}$ (arcsec)	$d_{\rm k2}$ (arcsec)	ν	$z_{\rm K2}$	$z_{\rm xray}$	σ_{v-xray} (km s^{-1})	$z_{\rm SIS}$	σ_v (km s^{-1})	$\chi^2_{\rm SIS}$	$z_{\rm NFW}$	$m_{\rm NFW}$ ($10^{14}\,M_\odot\,h^{-1}$)	m_{200} ($10^{14}\,M_\odot\,h^{-1}$)	$\chi^2_{\rm NFW}$
J022145.2-034617	35.438	−3.772	35.441	−3.772	35.456	−3.768	66.5	57.2	4.209	0.43	0.429 ± 0.001	977 ± 157	$0.34^{+0.11}_{-0.12}$	$766.1^{+182.5}_{-229.9}$	0.86	$0.35^{+0.15}_{-0.15}$	$2.04^{+2.78}_{-1.54}$	$1.79^{+2.44}_{-1.35}$	0.82
J022402.0-050525	36.008	−5.090	36.108	−5.088	36.077	−5.101	251.1	122.2	3.521	0.55	0.324 ± 0.001	364 ± 69	$0.20^{+0.17}_{-0.15}$	$344.8^{+97.5}_{-89.1}$	0.78	$0.20^{+0.18}_{-0.16}$	$0.23^{+0.06}_{-0.04}$	$0.20^{+0.05}_{-0.04}$	0.81
J022433.8-041405	36.141	−4.234	36.121	−4.165	36.097	−4.161	289.1	87.5	4.063	0.30	0.262 ± 0.001	483 ± 100	$0.26^{+0.13}_{-0.12}$	$359.6^{+131.2}_{-121.7}$	0.25	$0.25^{+0.11}_{-0.11}$	$0.77^{+0.17}_{-0.18}$	$0.67^{+0.15}_{-0.16}$	0.20
J022530.6-041420	36.377	−4.239	36.372	−4.258	36.372	−4.248	36.3	36.9	4.548	0.65	0.14 ± 0.002	899 ± 218	$0.65^{+0.26}_{-0.26}$	~ 0	5.69	$0.66^{+0.22}_{-0.20}$	~ 0	~ 0	4.63
J021837.0-054028	34.654	−5.675	34.655	−5.674	34.653	−5.626	175.7	170.7	4.186	0.33	0.275 ± 0.0	···	$0.31^{+0.14}_{-0.11}$	~ 0	4.18	$0.32^{+0.13}_{-0.10}$	~ 0	~ 0	3.87
J021842.8-053254	34.678	−5.548	34.657	−5.570	34.684	−5.572	91.1	98.4	4.194	0.36	0.38 ± 0.001	847 ± 279	$0.57^{+0.13}_{-0.14}$	$909.7^{+61.5}_{-60.1}$	1.55	$0.55^{+0.15}_{-0.13}$	$5.31^{+0.32}_{-0.30}$	$4.82^{+0.29}_{-0.27}$	1.47
J022632.4-050003	36.638	−5.007	36.678	−4.950	36.643	−4.959	62.6	72.8	3.156	0.22	0.494 ± 0.0	···	$0.23^{+0.19}_{-0.17}$	~ 0	3.80	$0.25^{+0.16}_{-0.21}$	~ 0	~ 0	3.81

Notes. K2 redshift denotes the median redshift of bright ($i \leqslant 20$) cluster members. X-ray redshift denotes the photometric redshifts of X-ray clusters (Adami et al. 2011). The parameters $d_{\rm xray}$ and $d_{\rm k2}$ are the offset between X-ray/optical and weak lensing center, respectively.

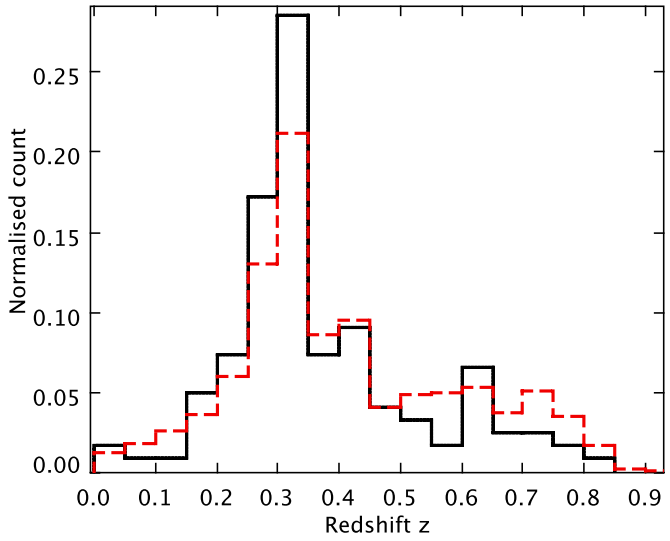

Figure 19. Cluster redshift distribution for the matched clusters of weak lensing and K2 (black solid histogram) and the total K2-detected clusters with K2 detection significance $(r - i) > 3$ (red dashed histogram).

(A color version of this figure is available in the online journal.)

Our tomographic analysis confirms the identification of 85 clusters with $\chi^2_{\rm red} = \chi^2/{\rm dof} < 3$. The mean redshift and velocity dispersion of these clusters are $\langle z_c \rangle = 0.36$ and $\langle \sigma_v \rangle = 658.8\,{\rm km\,s^{-1}}$. Their full properties are listed in Table 5. Reassuringly, we find that the inferred lens redshifts are effectively identical for either SIS or NFW profile fits, and are consistent (although noisy) with the (independent) photometric redshifts of the cluster member galaxies. Figure 22 compares the redshift estimates from tomographic gravitational lensing and optical spectroscopy of member galaxies for these 85 clusters.

At the faint end of our source galaxy sample, photo-z estimates will be unreliable because of noise in the photometry and degeneracies in the broad-band colors of galaxies with different spectral energy distributions at different redshifts. This will show up as a "double peak" in the posterior probability of the redshift distribution. Using only the best-fit peak might be randomly picking whichever of these peaks is higher because of noise. This often biases lensing analyses because the expected lensing signal may be much higher at one redshift than the other. To check for such an effect, we redo the tomographic analysis without any photo-zs that have a double peak (Arnouts et al. 2010). For cluster c3 in our catalog, we get very similar fit results: $z_{\rm SIS} = 0.26^{+0.13}_{-0.12}$ and $\sigma_v = 724.0^{+128.3}_{-131.5}$ for the SIS model, and $z_{\rm NFW} = 0.26^{+0.09}_{-0.11}$ and $m_{\rm NFW} = 4.14^{+0.81}_{-0.76}$ for the NFW model. This suggests that the fit is not very sensitive to that population of galaxies with "double peaks" in photometric redshifts.

In cases where the data are poorly fit ($\chi^2_{\rm red} > 3$) by a 3D lensing signal, the inferred velocity dispersion or virial mass are typically very small (often consistent with zero). These systems are probably spurious peaks due to noise or projection effects. In addition, two peaks (c71 and c104) have an unphysically high velocity dispersion $\sigma_{\rm tomo} > 1300\ {\rm km\ s^{-1}}$. After careful examination of the image data, we found that they lie near two strongly saturated stars whose flux extends beyond the masked regions, possibly degrading galaxy shape measurements.

One important goal of cluster lensing is to measure the total mass of systems, which can also be estimated from the velocity

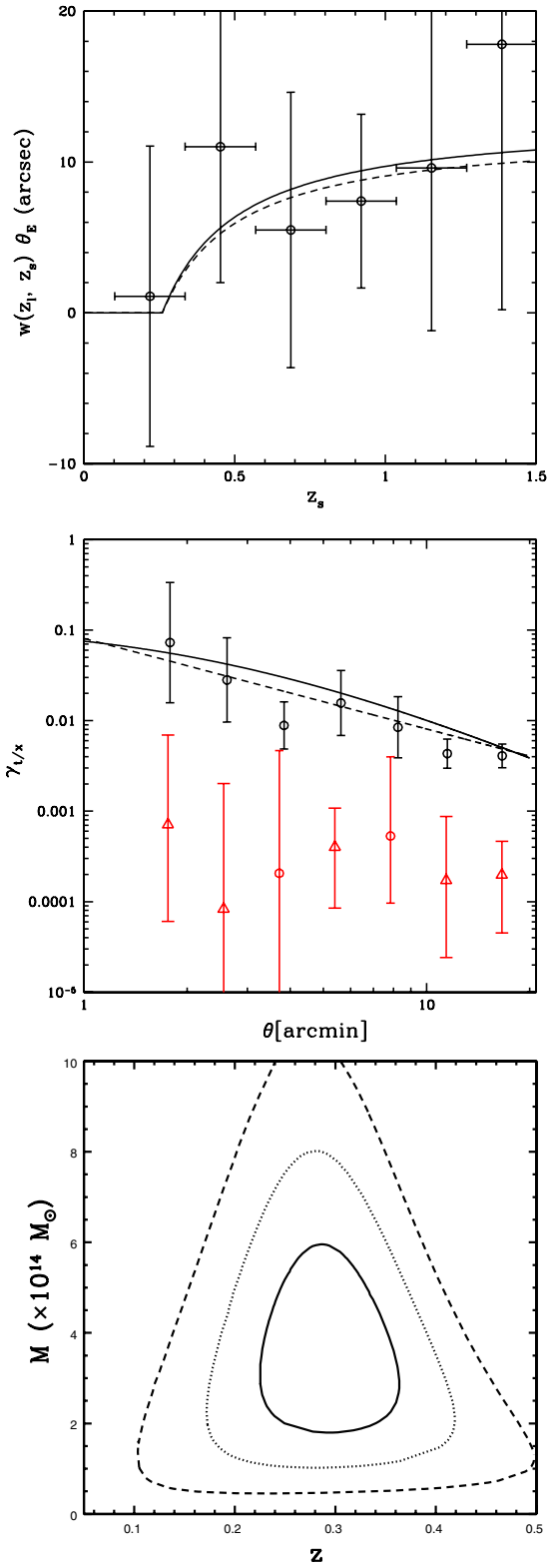

Figure 20. Results of a tomographic weak lensing analysis around one example peak (c3 in our catalog), which has an optical counterpart at redshift $z = 0.28$. The solid and dashed lines are the best-fit SIS and NFW models. Top: projection in the redshift direction showing the characteristic increase with redshift of a real signal. The best-fit lens redshift is $0.26^{+0.11}_{-0.10}$ for an SIS model and $0.26^{+0.12}_{-0.12}$ for an NFW model. Middle: radial profile projected onto the plane of the sky. Black circles show the E-mode tangential shear signal. Red circles (triangles) show positive (negative) values of the B-mode systematic signal, which oscillates about zero. Bottom: joint redshift-mass constraints from the best fit NFW model. Contours show 68%, 95%, and 99% confidence limits.

(A color version of this figure is available in the online journal.)

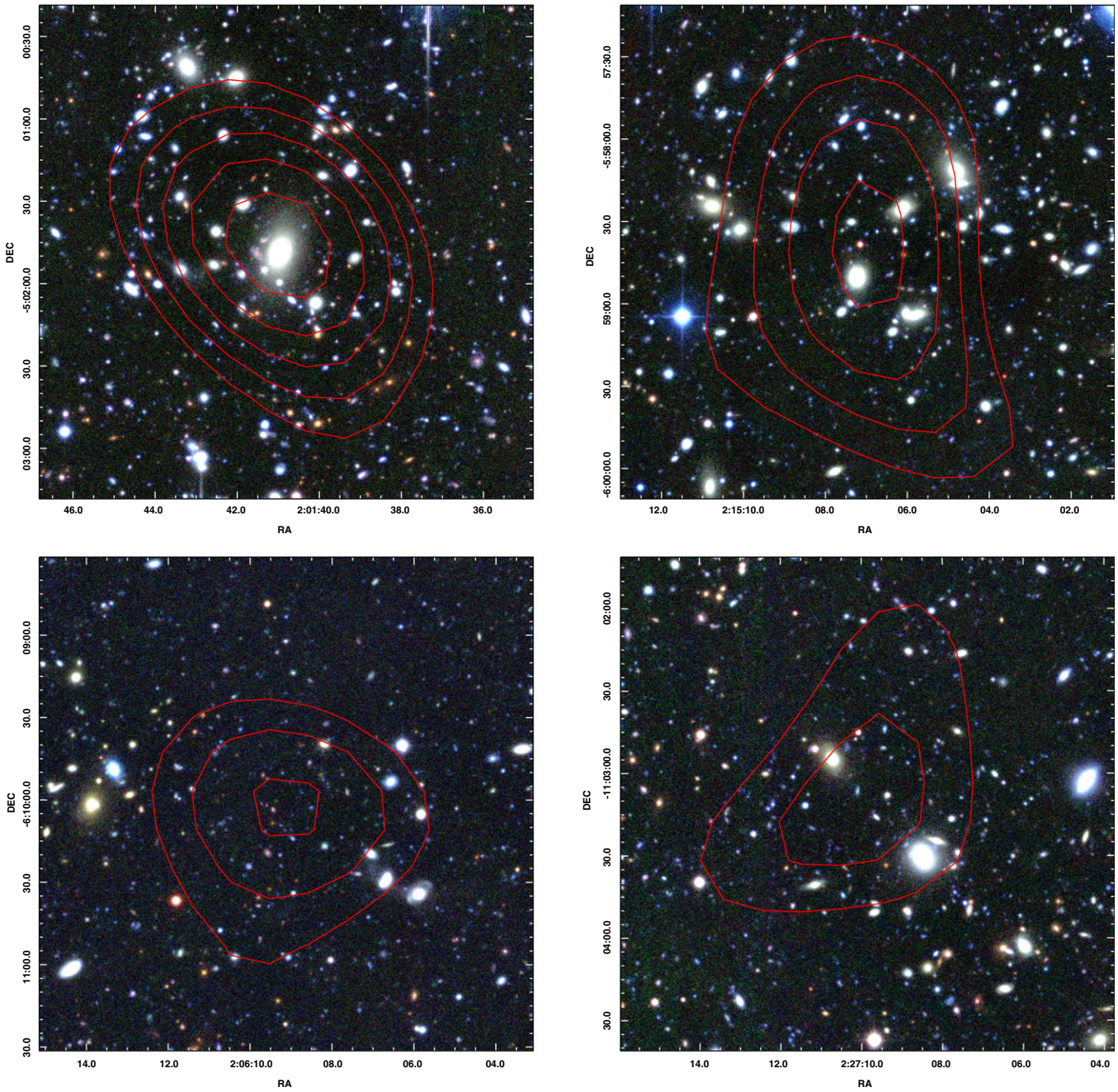

Figure 21. Composite 3 × 3 arcmin^2 CFHTLS g', r', i' color images for four clusters detected in both weak lensing and the K2 optical catalog. Contours show signal-to-noise in reconstructed convergence, starting at $\nu = 3.0$ and increasing in steps of 0.5 and the images are centered on the convergence peak. Top left: cluster c3 with $\nu = 5.395$. Top right: cluster c49 with $\nu = 4.728$. Bottom left: cluster c21 with $\nu = 4.142$. Bottom right: cluster c103 with $\nu = 3.725$. Candidate c21 is included here as an example of a 2D lensing peak that is probably spurious: it does not appear obviously associated with an overdensity of galaxies in the optical imaging, and is not well-fit by a 3D shear signal.

(A color version of this figure is available in the online journal.)

dispersion of its member galaxies or from its X-ray emission, under various assumptions about the state of the intracluster medium and hydrostatic equilibrium (e.g., Bahcall et al. 1995; Carlberg et al. 1996; Carlstrom et al. 2002).

Figure 23 shows the relation between one mass proxy obtained from X-ray observations and another obtained from weak lensing, for the four of seven clusters in our sample with an X-ray counterpart and an SIS velocity dispersion parameter well constrained by lensing. These are overlaid on the results of another lensing-selected cluster sample (Hamana et al. 2009) and two X-ray selected cluster samples (Cypriano et al. 2004; Hoekstra 2007). Even combining these samples, the scatter is large. However, the consistency of the scatter among the four samples suggests that neither detection method produces a strong selection bias. Note that, since the density (and shear) profile of real cluster is not necessarily a single power law, the best-fit SIS model may depend on details of the fitting method, and the range over which data are fit. Our results therefore are somewhat method-dependent. A corollary of this issue is that it might also be possible to minimize scatter in the

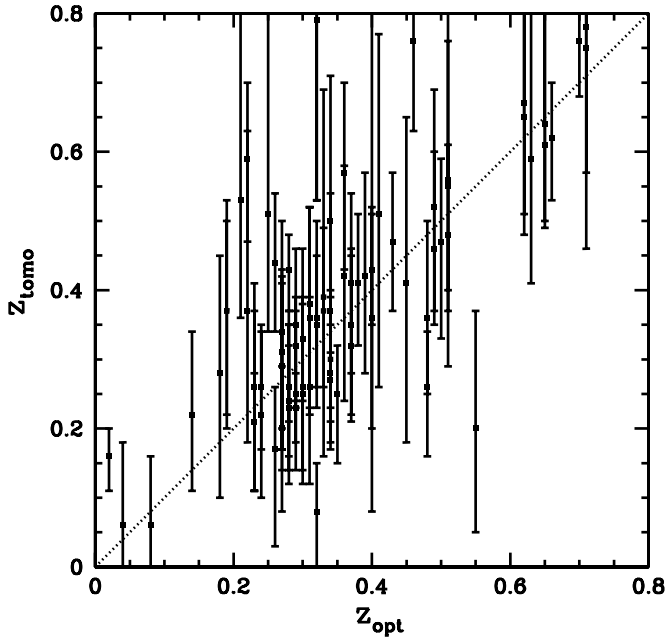

Figure 22. Comparison between cluster redshifts derived directly from the photometric redshifts of cluster member galaxies z_{opt} and from weak lensing tomography z_{tomo}. This figure includes all 85 $\nu > 3.5$ weak lensing peaks with optical counterparts, whose 3D shear signal is consistent at $\chi^2_{red} < 3$ with the expected increase as a function of redshift.

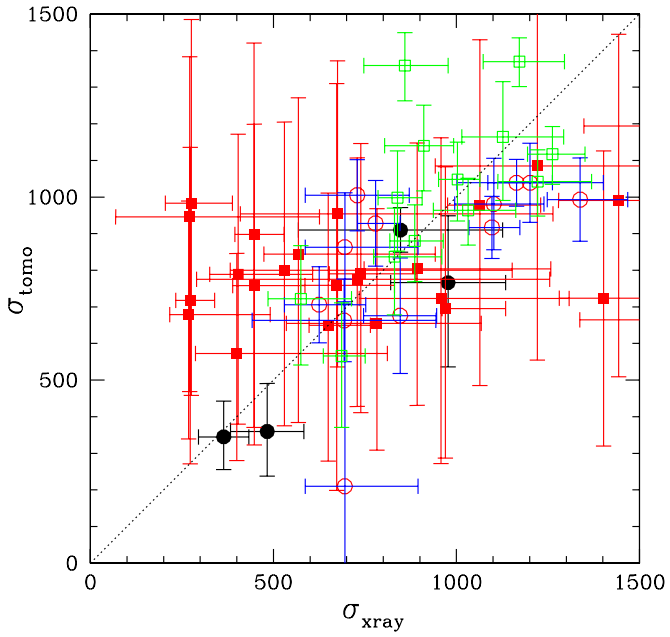

Figure 23. Scaling relation between X-ray and weak lensing tomographic measurements of the velocity dispersion of clusters. Black filled circles show our data for four lensing-selected clusters. Red filled squares show the lensing-selected clusters of Hamana et al. (2009). Blue open circles and green open squares denote the X-ray selected clusters from Cypriano et al. (2004) and Hoekstra (2007), respectively.

(A color version of this figure is available in the online journal.)

σ_{xray}–σ_{tomo} relation by optimizing the tomographic lens fitting method.

7. CONCLUSIONS

We have presented a tomographic weak gravitational lensing analysis of the completed 64 deg^2 CFHTLS-Wide W1 field, demonstrating some of the power of lensing to probe mass in galaxy clusters. We measured the shapes of distant galaxies using the KSB shape measurement method, which we verified against shape measurements from high-resolution *HST* imaging of an overlapping sky area. We also obtained consistent shape measurements using two independent imaging bands. The level of residual shape measurement systematics is an order of magnitude lower than the 1%–10% shear signal expected in galaxy clusters, so this analysis is acceptable for cluster studies.

We have reconstructed the largest contiguous "dark matter map" convergence field to date, using two different smoothing scales to help remove spurious noise peaks. From this map, we performed the largest lensing-selected blind cluster search to date, finding 301 local maxima in the lensing map with detection significance $\nu > 3.5$. Once sources of noise are properly modeled from the intrinsic shapes of galaxies and substructure, this is consistent with predictions from a ΛCDM cosmology. Note that our theoretical calculations (Fan et al. 2010) do not consider projection effects of structures along the line of sight.

To identify counterparts of the weak lensing peaks, we match our cluster candidates to the K2 galaxy cluster catalog, created using photometric redshift estimates across the CFHTLS-Wide W1 field (Thanjavur et al. 2009). Of the 301 peaks with $\nu > 3.5$, 126 have a corresponding optically detected BCG within 3.′0. In the (much smaller) survey area that overlaps the XMM-LSS survey, we also find matches for seven lensing peaks with X-ray selected clusters. Thus, many of the candidate peaks are indeed likely just noise.

Tomographic weak lensing techniques dramatically improve standard 2D algorithms. In a full 3D lensing analysis of the $\nu > 3.5$ peaks, we further distinguish real clusters from noise fluctuations, and confirm (at $\chi^2_{red} < 3$) the identification of 85 clusters. Importantly, we obtain independent measurements of the cluster lens redshifts, which are consistent with the redshifts of their previously identified optical counterparts. For each cluster, we fit NFW and SIS radial profiles to the lensing data to measure the mass or velocity dispersion σ_{tomo}. The clusters' mean redshift and velocity dispersion is $\langle z_c \rangle = 0.36$ and $\langle \sigma_c \rangle = 658.8$ km s^{-1}. Weak lensing measurements of the total mass in the four of our clusters with X-ray counterparts are also in reasonable agreement with mass estimates obtained from X-ray emission. Future surveys, such as DES, LSST, KDUST, and EUCLID, will be able to apply these techniques to map clusters in much larger volumes. Such large catalogs will also be able to tightly constrain cosmological models (Takada & Bridle 2007; Dietrich & Hartlap 2010).

The authors thank Bernard Fort, Liping Fu, Bo Qin, Catherine Heymans, and Ludovic Van Waerbeke for useful discussions. H.Y.S. acknowledges support from the Sino French laboratories FCPPL and Origins, and CPPM hospitality during stays in France. H.Y.S. acknowledges the support from NSFC of China under grants 11103011 and China Postdoctoral Science Foundation. J.P.K. acknowledges supports from CNRS as well as PNCG and CNES. Z.H.F. acknowledges the support from NSFC of China under grants 10773001, 11033005, and 973 program 2007CB815401. M.L. acknowledges the Centre National de la Recherche Scientifique (CNRS) for its support. The Dark Cosmology Centre is funded by the Danish National Research Foundation.

This work is based on observations obtained with MegaPrime/MegaCam, a joint project of CFHT and

CEA/DAPNIA, at the Canada–France–Hawaii Telescope (CFHT) which is operated by the National Research Council (NRC) of Canada, the Institut National des Science de l'Univers of the Centre National de la Recherche Scientifique (CNRS) of France, and the University of Hawaii. This work is based in part on data products produced at TERAPIX and the Canadian Astronomy Data Centre as part of the Canada–France–Hawaii Telescope Legacy Survey, a collaborative project of NRC and CNRS.

This work also uses observations obtained with the *Hubble Space Telescope*. The HST COSMOS Treasury program was supported by the NASA grant HST-GO-09822. We thank Tony Roman, Denise Taylor, and David Soderblom for their assistance in planning and scheduling the extensive COSMOS observations. We thank the NASA IPAC/IRSA staff (Anastasia Laity, Anastasia Alexov, Bruce Berriman, and John Good) for providing online archive and server capabilities for the COSMOS data sets. It is also our pleasure to gratefully acknowledge the contributions of the entire COSMOS collaboration, consisting of more than 70 scientists. More information on the COSMOS survey is available at http://www.astro.caltech.edu/cosmos.

REFERENCES

Adami, C., Mazure, A., Pierre, M., et al. 2011, A&A, 526, 18
Arnouts, S., Coupon, J., Ilbert, O., et al. 2010, Photometric Redshifts of the CFHTLS-Wide T0006 Release v1.0
Bacon, D. J., Massey, R. J., Refregier, A. R., & Ellis, R. S. 2003, MNRAS, 344, 673
Bahcall, N. A., Lubin, L. M., & Dorman, V. 1995, ApJ, 447, L81
Bardeau, S., Kneib, J.-P., Czoske, O., et al. 2005, A&A, 434, 433
Bardeau, S., Soucail, G., Kneib, J.-P., et al. 2007, A&A, 470, 449
Bardeen, J. M., Bond, J. R., Kaiser, N., & Szalay, A. S. 1986, ApJ, 304, 15
Bartelmann, M., Doran, M., & Wetterich, C. 2006, A&A, 454, 47
Bertin, E., & Arnouts, S. 1996, A&AS, 117, 393
Bode, P., Ostriker, J. P., Weller, J., & Shaw, L. 2007, ApJ, 663, 139
Bond, J. R., & Efstathiou, G. 1987, MNRAS, 226, 655
Bridle, S., Balan, S. T., Bethge, M., et al. 2010, MNRAS, 405, 2044
Bullock, J. S., Kolatt, T. S., Sigad, Y., et al. 2001, MNRAS, 321, 559
Carlberg, R. G., Yee, H. K. C., Ellingson, E., et al. 1996, ApJ, 462, 32
Carlstrom, J. E., Holder, G. P., & Reese, E. D. 2002, ARA&A, 40, 643
Coupon, J., Ilbert, O., Kilbinger, M., et al. 2009, A&A, 500, 981
Crittenden, R. G., Natarajan, P., Pen, U.-L., & Theuns, T. 2002, ApJ, 568, 20
Cypriano, E. S., Sodre, L., Jr., Kneib, J.-P., & Campusano, L. E. 2004, ApJ, 613, 95
Dahle, H., Pedersen, K., Lilje, P. B., Maddox, S. J., & Kaiser, N. 2003, ApJ, 591, 662
Dietrich, J. P., Erben, T., Lamer, G., et al. 2007, A&A, 470, 812
Dietrich, J. P., & Hartlap, J. 2010, MNRAS, 402, 1049
Eke, V. R., Cole, S., & Frenk, C. S. 1996, MNRAS, 282, 263
Fan, Z. H., Shan, H. Y., & Liu, J. Y. 2010, ApJ, 719, 1408
Francis, M. J., Lewis, G. F., & Linder, E. V. 2009, MNRAS, 394, 605
Frenk, C. S., White, S. D. M., Efstathiou, G., & Davis, M. 1990, ApJ, 351, 10
Fu, L., Semboloni, E., Hoekstra, H., et al. 2008, A&A, 479, 9
Gavazzi, R., Adami, C., Durret, F., et al. 2009, A&A, 498, 33
Gavazzi, R., & Soucail, G. 2007, A&A, 462, 459
Geller, M. J., Kurtz, M. J., Dell'Antonio, I. P., Ramella, M., & Fabricant, D. G. 2010, ApJ, 709, 832
Goranova, Y., Hudelot, P., Magnard, F., et al. 2009, The CFHTLS T0006 Release, http://terapix.iap.fr/cplt/T0006-doc.pdf
Grossi, M., & Springel, V. 2009, MNRAS, 394, 1559
Haiman, Z., Wang, S., Khoury, J., et al. 2004, AAS, 36, 1529
Hamana, T., Miyazaki, S., Kashikawa, N., et al. 2009, PASJ, 61, 833
Hamana, T., Takada, M., & Yoshida, N. 2004, MNRAS, 350, 893
Hennawi, J. F., & Spergel, D. N. 2005, ApJ, 624, 59
Hetterscheidt, M., Erben, T., Schneider, P., et al. 2005, A&A, 442, 43
Heymans, C., Van Waerbeke, L., Bacon, D., et al. 2006, MNRAS, 368, 1323
Hoekstra, H. 2007, MNRAS, 379, 317
Hoekstra, H., Franx, M., & Kuijken, K. 2000, ApJ, 532, 88
Hoekstra, H., Franx, M., Kuijken, K., & Squires, G. 1998, ApJ, 504, 636
Hoekstra, H., Mellier, Y., Van Waerbeke, L., et al. 2006, ApJ, 647, 116
Ilbert, O., Arnouts, S., McCracken, H., et al. 2006, A&A, 457, 841
Jain, B., & Van Waerbeke, L. 2000, ApJ, 530, L1
Jiao, Y. X., Shan, H. Y., & Fan, Z. H. 2011, RAA, 11, 507
Johnston, D. E., Sheldon, E., Wechsler, R., et al. 2007, arXiv:0709.1159
Kaiser, N., & Squires, G. 1993, ApJ, 404, 441
Kaiser, N., Squires, G., & Broadhurst, T. 1995, ApJ, 449, 460
Kaiser, N., Wilson, G., & Luppino, G. A. 2000, arXiv:astro-ph/0003338
Kasliwal, M., Massey, R., Ellis, R., Miyazaki, S., & Rhodes, J. 2008, ApJ, 684, 34
Leauthaud, A., Finoguenov, A., Kneib, J.-P., et al. 2010, ApJ, 709, 97
Leauthaud, A., Massey, R., Kneib, J.-P., et al. 2007, ApJS, 172, 219
Luppino, G. A., & Kaiser, N. 1997, ApJ, 475, 20
Mandelbaum, R., Hirata, C. M., Seljak, U., et al. 2005, MNRAS, 361, 1287
Mandelbaum, R., Seljak, U., Cool, R. J., et al. 2006, MNRAS, 372, 758
Massey, R., Heymans, C., Berge, J., et al. 2007, MNRAS, 376, 13
Massey, R., Réfrégier, A., Bacon, D., Ellis, R., & Brown, M. 2005, MNRAS, 359, 1277
Maturi, M., Schirmer, M., Meneghetti, M., Bartelmann, M., & Moscardini, L. 2007, A&A, 462, 473
Miyazaki, S., Hamana, T., Shimasaku, K., et al. 2002, ApJ, 580, L97
Miyazaki, S., Hamana, T., Ellis, R. S., et al. 2007, ApJ, 669, 714
Navarro, J. F., Frenk, C. S., & White, S. D. M. 1996, ApJ, 462, 563
Pacaud, F., Pierre, M., Adami, C., et al. 2007, MNRAS, 382, 1289
Pires, S., Starck, J.-L., Amara, A., Refregier, A., & Teyssier, R. 2009, A&A, 505, 969
Press, W. H., & Schechter, P. 1974, ApJ, 187, 425
Schirmer, M., Erben, T., Hetterscheidt, M., & Schneider, P. 2007, A&A, 462, 875
Schirmer, M., Erben, T., Schneider, P., et al. 2003, A&A, 407, 869
Schneider, P., van Waerbeke, L., & Mellier, Y. 2002, A&A, 389, 729
Scoville, N., Abraham, R. G., Aussel, H., et al. 2007, ApJS, 172, 38
Semboloni, E., Mellier, Y., van Waerbeke, L., et al. 2006, A&A, 452, 51
Shan, H. Y., Qin, B., Fort, B., et al. 2010, MNRAS, 406, 1134
Sheth, R. K., & Tormen, G. 1999, MNRAS, 308, 119
Starck, J. L., Pires, S., & Réfrégier, A. 2006, A&A, 451, 1139
Takada, M., & Bridle, S. 2007, New J. Phys., 9, 446
Tang, J. Y., & Fan, Z. H. 2005, ApJ, 635, 60
Thanjavur, K., Willis, J., & Crampton, D. 2009, ApJ, 706, 571
Van Waerbeke, L. 2000, MNRAS, 313, 524
White, M., van Waerbeke, L., & Mackey, J. 2002, ApJ, 575, 640
Wittman, D., Dell'Antonio, I. P., Hughes, J. P., et al. 2006, ApJ, 643, 128
Wittman, D., Margoniner, V. E., Tyson, J. A., et al. 2003, ApJ, 597, 218
Wittman, D., Tyson, J. A., Margoniner, V. E., Cohen, J. G., & Dell'Antonio, I. P. 2001, ApJ, 557, L89